



VYSOKÉ UČENÍ TECHNICKÉ V BRNĚ

BRNO UNIVERSITY OF TECHNOLOGY



FAKULTA STROJNÍHO INŽENÝRSTVÍ
ENERGETICKÝ ÚSTAV

FACULTY OF MECHANICAL ENGINEERING
ENERGY INSTITUTE

VLIV ZAKONČENÍ VÝZTUŽNÉ LOPATKY U FRANCISOVY TURBÍNY NA TVORBU KÁRMÁNOVÝCH VÍRŮ

INFLUENCE OF THE FRANCIS TURBINE STAY VANE TRAILING EDGE SHAPE
ON GENERATION OF KARMAN VORTEX STREET

DIPLOMOVÁ PRÁCE
MASTER'S THESIS

AUTOR PRÁCE
AUTHOR

Bc. VOJTĚCH NOVOTNÝ

VEDOUCÍ PRÁCE
SUPERVISOR

doc. Ing. PAVEL RUDOLF, Ph.D.

BRNO 2015

Vysoké učení technické v Brně, Fakulta strojního inženýrství

Energetický ústav

Akademický rok: 2014/2015

ZADÁNÍ DIPLOMOVÉ PRÁCE

student(ka): Bc. Vojtěch Novotný

který/která studuje v **magisterském navazujícím studijním programu**

obor: **Fluidní inženýrství (2301T036)**

Ředitel ústavu Vám v souladu se zákonem č.111/1998 o vysokých školách a se Studijním a zkušebním řádem VUT v Brně určuje následující téma diplomové práce:

Vliv zakončení výztužné lopatky u Francisovy turbíny na tvorbu Kármánových vírů

v anglickém jazyce:

Influence of the Francis turbine stay vane trailing edge shape on generation of Karman vortex street

Stručná charakteristika problematiky úkolu:

Za špatně obtékanými tělesy vzniká pravidelné odtrhávání vírů známé jako Kármánova vírová stezka. Periodická změna tlakového pole vyvolaná Kármánovou stezkou silově budí obtékanou konstrukci a může způsobit její poškození. K tomu dochází např. u komínů, stožárů ale také lopatek tepelných i vodních turbín.

Cíle diplomové práce:

Cíle diplomové práce lze rozdělit do tří kroků:

- naladění výpočtového modelu na výsledcích experimentálního obtékání kvádry
- výpočet Kármánovy vírové stezky na osamoceném hydraulickém profilu, testování vlivu tvaru výstupní hrany na amplitudově-frekvenční charakteristiku tlaku za profilem
- výpočet Kármánovy vírové stezky za radiální lopatkovou mříží výztužných lopatek Francisovy turbíny, nalezení optimálního tvaru odtokové hrany

Seznam odborné literatury:

- [1] Dörfler, P., Sick, M., Coutu, A.: Flow-induced pulsation and vibration in hydroelectric machinery, Springer, 2012
- [2] Bajer, J.: Mechanika 3, Nakladatelství RNDr. V. Chlup, 2012
- [3] Vu, T., Nennemann, B., Ausoni, P., Farhat, M., Avellan, F.: Unsteady CFD Prediction of von Kármán Vortex Shedding in Hydraulic Turbine Stay Vanes, Proc. of Hydro 2007, 2007
- [4] Zobeiri, A.: Effect of Hydrofoil Trailing Edge Geometry on the Wake Dynamics, EPFL PhD thesis, Lausanne, 2012

Vedoucí diplomové práce: doc. Ing. Pavel Rudolf, Ph.D.

Termín odevzdání diplomové práce je stanoven časovým plánem akademického roku 2014/2015.

V Brně, dne 21. 11. 2014

L.S.

doc. Ing. Jiří Pospíšil, Ph.D.
Ředitel ústavu

doc. Ing. Jaroslav Katolický, Ph.D.
Děkan fakulty

ABSTRAKT

Za špatně obtékanými tělesy vzniká v určitém rozsahu rychlostí pravidelné odtrhávání vírů známé jako von Kármánova vírová stezka. Tento fenomén může mít nepříznivý vliv na obtékanou konstrukci, neboť způsobuje periodickou změnu tlakového pole a silově tak na konstrukci působí. Je-li frekvence odtrhávání vírů blízká vlastní frekvenci obtékané konstrukce, může dojít k samobuzenému kmitání a v extrémním případě až k únavovému lomu. V případě vodních turbín je tento jev častý u výztužných lopatek. Tvarem odtokové hrany lopatky lze ovlivnit jak frekvenci odtrhávání vírů, tak amplitudu vztahové síly působící na lopatku. Cílem této diplomové práce je pomocí CFD výpočtu najít optimální tvar odtokové hrany výztužné lopatky pro konkrétní Francisovu turbínu.

ABSTRACT

In the flow past bluff bodies for a certain range of velocity a periodical vortex shedding emerges which is known as von Kármán vortex street. This phenomenon causes the periodical alteration of pressure field which affects the body. Should the vortex shedding frequency be similar to the body natural frequency, the amplitude of vibration significantly increases which can lead to fatigue cracking. In the case of water turbines, this phenomenon often affects the stay vanes. Both the vortex shedding frequency and the lift force amplitude can be influenced by the modification of the trailing edge geometry. The aim of this thesis is to use CFD computation in order to find the optimal geometry of the stay vane trailing edge for the specific Francis turbine unit.

KLÍČOVÁ SLOVA

špatně obtékaná tělesa, von Kármánova vírová stezka, frekvence odtrhávání, vibrace indukovaná víry, fenomén lock-in, vodní turbína, výztužná lopatka, odtoková hrana, únavový lom, Strouhalovo číslo, CFD výpočet

KEY WORDS

flow past bluff bodies, von Kármán vortex street, shedding frequency, vortex induced vibration, lock-in phenomenon, water turbine, stay vane, trailing edge, fatigue crack, Strouhal number, CFD simulation

BIBLIOGRAFICKÁ CITACE

NOVOTNÝ, V. *Vliv zakončení výztužné lopatky u Francisovy turbíny na tvorbu Kármánových vírů*. Brno: Vysoké učení technické v Brně, Fakulta strojního inženýrství, 2015. 72 s. Vedoucí diplomové práce doc. Ing. Pavel Rudolf, Ph.D.

PROHLÁŠENÍ

Prohlašuji, že jsem diplomovou práci na téma *Vliv zakončení výztužné lopatky u Francisovy turbíny na tvorbu Kármánových vírů* vypracoval samostatně s použitím odborné literatury a dostupných pramenů uvedených v seznamu použité literatury.

V Brně dne 25. 5. 2015

.....
Vojtěch Novotný

PODĚKOVÁNÍ

Děkuji panu doc. Ing. Pavlu Rudolfovi, Ph. D. za jeho nadhled a nadšení pro věc.

Dále děkuji společnosti ČKD Blansko Engineering, a.s. za zadání diplomové práce a za poskytnutí geometrie výztužné lopatky.

TABLE OF CONTENTS

1	INTRODUCTION	15
I	THE PROBLEM OVERVIEW	17
2	VON KÁRMÁN VORTEX STREET	17
2.1	Flow past Circular Cylinder	20
2.2	Strouhal Number	21
2.3	Lock-in Condition	22
3	STAY VANE CRACKING	25
II	CFD SIMULATIONS.....	29
4	FLOW PAST SQUARE CYLINDER	31
4.1	Experiment by Lyn	31
4.2	CFD Simulation of flow past Square Cylinder.....	31
4.2.1	2D Simulation	32
4.2.2	3D Simulation	35
4.3	CFD Results.....	37
5	FLOW PAST NACA 0009 HYDROFOIL	43
5.1	Experiment by Zobeiri.....	43
5.1.1	Test Rig	43
5.1.2	Experimental Hydrofoil	43
5.1.3	Experiment Results	45
5.2	CFD Simulation of flow past NACA 0009 Hydrofoil.....	47
5.2.1	2D Simulation	47
5.2.2	3D Simulation	49
5.3	CFD Results.....	50
6	ČBE ASSIGNMENT	59
6.1	CFD Simulation of ČBE Assignment.....	59
6.2	CFD Results.....	61
III	CONCLUSION AND PERSPECTIVES	65
7	CONCLUSION.....	65
8	PERSPECTIVES	67
	ABBREVIATIONS AND SYMBOLS USED	69
	REFERENCES	71

1 INTRODUCTION

Some solid bodies cause, when placed into a stream of a fluid, the separation of boundary layers on their surfaces which continues to be present in their wake. These are usually referred to as bluff bodies. At very low Reynolds number the flow past such bodies is stable, however when the critical value of Reynolds number is reached, instability develops. The instability is caused by two shear layers formed by the detachment of boundary layers on both upper and lower surfaces. These shear layers generate a vortex shedding from alternate body surfaces creating row of vortices in the body wake. This alternate vortex shedding is known as von Kármán vortex street. Since the asymmetric formation of vortices causes periodic alteration of pressure field, it is responsible for fluctuating lift force transverse to the flow that affects the body. [4]

Such vibration of a structure is particularly dangerous when the frequency of vortex shedding coincides with the natural frequency of the structure or more precisely with the natural frequency of fluid-structure system. In that case the amplitude of vibration significantly amplifies which can cause fatigue cracks and lead to premature failure of the structure.

In case of hydro power plants the potentially most endangered parts (when speaking of vortex streets) are runner blades and stay vanes. Dörfler [7] mentions that vortex induced vibration of guide vanes is more seldom, but has also been observed in some machines. The vortex shedding frequency and the lift amplitude, concerning vanes and blades, can be changed by the modification of their trailing edge geometry. The aim of the modification is to reduce the lift coefficient and change the vortex shedding frequency so that it would not coincide with the natural frequency of the fluid-structure system.

Such an optimization of the stay vane trailing edge geometry is the subject of this thesis. As Gummer [13] says: “One of the first reported incidents of stayvane cracking was described by Goldwag and Berry in 1968; since then, every year more literature on various aspects of the subject has been published. It would appear, therefore, that the problem of vortex-induced cracking of stayvanes is one long since resolved: however, this is not the case.”

The thesis is written in cooperation with ČKD Blansko Engineering, a.s., the member of Litostroj Power group, who provided the stay vane geometry and the inlet-velocity profile necessary for computing.

The thesis is divided into three parts. The first part (The Problem Overview) describes the current state of art concerning von Kármán vortex street phenomenon and the resulting stay vane cracking in a qualitative way.

The second part (CFD Simulations) describes the problem in rather quantitative way. It consists of two test cases and of the solution of the ČBE (ČKD Blansko Engineering) assignment. The test cases should serve as an instrument for suitable CFD solver setting. The first test case is a simple one, dealing with the flow past square cylinder based on Lyn's experiment [17]. The second test case which deals with the flow past NACA 0009 hydrofoil is based on Zobeiri's experiment [24] and primarily examines the solver's sensitivity towards the trailing edge geometry modification. The solution of the ČBE assignment is subsequently carried out on the basis of the results from these two test cases.

The last part (Conclusion and Perspectives) resumes the results and presents possibilities for further study and research.

I THE PROBLEM OVERVIEW

2 VON KÁRMÁN VORTEX STREET

In the flow behind a bluff body there is pair of counter-rotating vortices formed, which stays just behind the body. When the velocity of the flow increases, the vortices begin to shed and are carried away with the flow. With increasing velocity the flow becomes turbulent and the structure of eddies irregular. At a certain span of velocity (for the Reynolds number $Re \approx 10^2$) the periodic shedding of vortices is present which forms a stable pattern of two rows of alternating vortices that are carried downstream with the flow. Such a pattern is termed von Kármán vortex street after Theodore von Kármán, Hungarian mathematician and physicist (1881 – 1963). [1] [3]

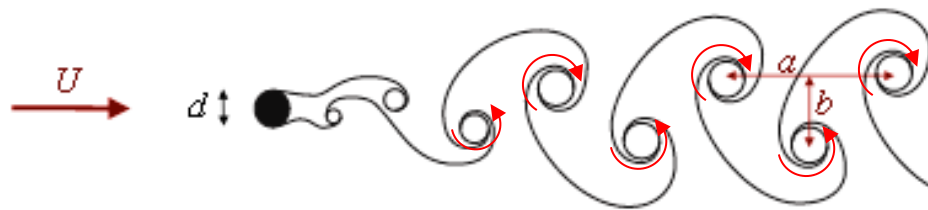


Fig. 2.1 Sketch of von Kármán vortex street [8]

However, von Kármán was not the first one who described the phenomenon. Already in 1878 Czech physicist Vincenc Strouhal (1850 – 1922) observed the flow of wind past telegraph lines and described the relation between the vibration frequency and the wind velocity. Strouhal defined the dependency of the pitch of the tunes produced by the lines on the wind velocity and the wire diameter. The oscillations of the wires were formerly known as *Strouhal's frictional tunes*. Later the vortex structure was described and the pictures of it were published in 1908 by French physicist Henri Bénard (1874 – 1939), who observed the phenomenon in viscous fluids. Finally in 1911 Theodore von Kármán proposed the mathematical theory of the vortices and contributed to the knowledge of the topic. He found that the vortex structure is stable only for a certain ratio of cross-stream and stream-wise vortex spacing. This ratio being $b/a \approx 0.2806$, where b is the cross-stream distance of the two rows and a is the stream-wise distance of juxtaposed vortices, see Figure 2.1. [1] [3]

Von Kármán vortex street is a widespread phenomenon that can be found in a wide range of situations and scales. The core diameter of a vortex can range from millimeters in case of flow past narrow air/hydrofoil to hundreds of meters in case of wind that blows past solitary island in the ocean and leaves a picturesque vortex track in the clouds. This can be observed e.g. in case of Guadalupe Island which is situated about 240 km off the west coast of Mexico, see Figure 2.2.

However, von Kármán vortex street does not impact only on airfoils or islands. It can affect smokestacks, broadcast towers, tall buildings, bridges, marine propellers

and last but not least runner blades, guide vanes and stay vanes of hydropower plants. Usually the phenomenon is accompanied by loud noise that is often referred to as “singing”. [7]



Fig. 2.2 Vortex street behind Guadalupe Island [14]

Despite rather peacefully looking structure of the vortex street and the singing mentioned above, von Kármán vortices are, at least in technical applications, unwanted and potentially dangerous.

The vortex street pattern is caused by the separation of the boundary layer on both upper and lower surfaces of the body. According to Gerrard, a key factor in the formation of a vortex-street wake is the mutual interaction between the two separating shear layers. It is said that a vortex continues to grow, fed by circulation from its connected shear layers, until it is strong enough to draw the opposing shear layers across the near wake. The approach of oppositely signed vorticity, in sufficient concentration, cuts off further supply of circulation to the growing vortex, which is then shed and moves off downstream. [11]

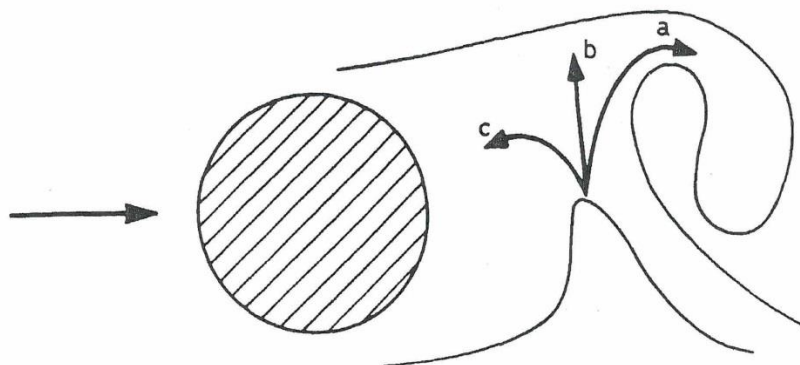


Fig. 2.3 Sketch of vortex-formation model [11]

Gerrard’s sketch (Figure 2.3) shows the vortex-formation model in which the entrainment processes play an important role. Entrained fluid (a) is engulfed into the growing vortex while (b) finds its way into the developing shear layer. The near-

wake region between the base of the body and the growing vortex oscillates in size, and some further fluid, (c), is temporarily entrained to it. Bearman says that it is the presence of two shear layers, rather than the bluff body itself, that is primarily responsible for vortex shedding. [4]

The potential danger of the phenomenon is a consequence of the asymmetric formation of the vortices behind the body. As a result of the alternating eddy formation, the body – a rod, a plate or in case of water turbines, stay vanes, or runner blades – behind which the vortex street occurs is a subject to a periodical reaction force (caused by pulsating pressure field) transverse to the flow pulsating with the frequency of eddy detachment. The frequency of vortex shedding may coincide with a natural frequency of the body producing it, resulting in a resonant vibration and this may cause large amplitudes. The frequency is generally high and as a result a large number of cycles may occur leading to a mechanical damage from high cycle fatigue. [7]

Vortex shedding frequency and the shape of eddy formation depends on the body dimensions, the fluid density ρ , the fluid dynamic viscosity μ and the free stream velocity C_{ref} . These factors are usually presented in the form of dimensionless Reynolds number Re :

$$Re = \frac{\rho * C_{ref} * D}{\mu} = \frac{C_{ref} * D}{\nu} \quad (2.1)$$

where D is a characteristic body dimension (e.g. diameter in case of a circular cylinder) and ν is a kinematic viscosity of the fluid. Different patterns for specific Reynolds numbers are presented in Figure 2.4.

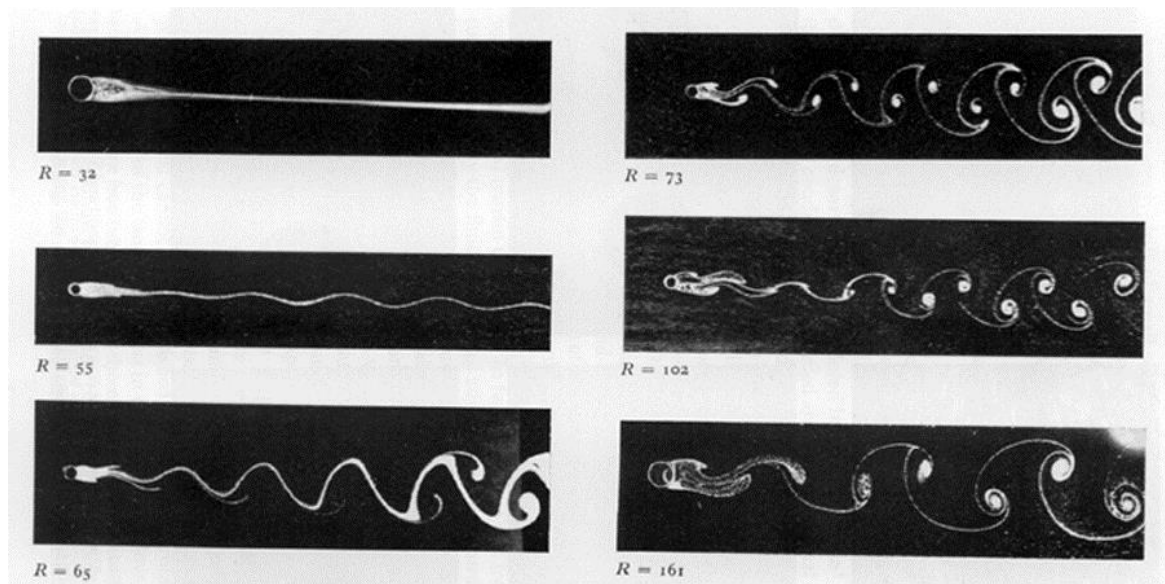


Fig. 2.4 Vortex street regimes for specific Reynolds numbers [6]

In a number of sources there can be found that the vortex shedding frequency also depends on the body surface roughness Ra and recent studies have shown that also cavitation has an influence on the shedding frequency and the resulting vibration behavior. [7] [1]

2.1 Flow past Circular Cylinder

Theodore von Kármán presented his work on the case of a cylinder with circular cross-section and the majority of following experimental work in this area is related to vortex shedding from cylinders. Therefore the uniform flow past a circular cylinder is the “benchmark configuration” for investigation of vortex shedding and has been extensively studied experimentally by different authors. [1] [4] [7]

Here, Figure 2.5 shows the overview of the regimes for incompressible flow presented by Schlichting. [19]






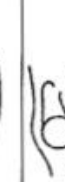

Reynolds number $Re = Vd/\nu$ Strouhal number $Sr = fd/V$		Flow regime	Flow form	Flow characteristic	Strouhal number Sr	Drag coefficient c_D
$Re \rightarrow 0$		Creeping flow		Steady, no wake	–	see Fig. 1.12
$3 - 4 < Re < 30 - 40$		Vortex pairs in wake		Steady, symmetric separation	–	$1.59 < c_D < 4.52$ ($Re = 30$) ($Re = 40$)
$30 < Re < 80$ $40 < Re < 90$		Onset of Karman vortex street		Laminar, unstable wake	–	$1.17 < c_D < 1.59$ ($Re = 100$) ($Re = 30$)
$80 < Re < 150$ $90 < Re < 300$		Pure Karman vortex street		Karman vortex street	$0.14 < Sr < 0.21$	
$150 < Re < 10^5$ $300 < Re < 1.3 \cdot 10^5$		Subcritical regime		Laminar, with vortex street instabilities	$Sr = 0.21$	$c_D \approx 1.2$
$10^5 < Re < 3.5 \cdot 10^6$ $1.3 \cdot 10^5 < Re < 3.5 \cdot 10^6$		Critical regime		Laminar separation Turbulent reattachment Turbulent separation Turbulent wake	No preferred frequency	$0.2 < c_D < 1.2$
$3.5 \cdot 10^6 < Re$		Supercritical regime (transcritical)		Turbulent separation	$0.25 < Sr < 0.30$	$c_D \approx 0.6$

Fig. 2.5 Incompressible flow regimes at circular cylinder [19]

2.2 Strouhal Number

The shedding frequency is often presented by means of normalized frequency, or Strouhal number, which is defined as:

$$St = \frac{f_s * D}{C_{ref}} \quad (2.2)$$

where St (sometimes labeled Sh or St_h) is dimensionless Strouhal number, f_s is a vortex shedding frequency, C_{ref} is a free stream velocity and D a characteristic body dimension. [16]

Strouhal number has been measured experimentally by various authors. According to these authors the Strouhal number values are usually in the range 0.15 – 0.3 [23] or more precisely 0.18 – 0.24 [7] or possibly 0.16 – 0.19 [13].

According to Locky [16], Strouhal number depends on:

- geometry (cylinder or blade)
- local Reynolds number (laminar flow, transition range or fully turbulent flow)
- trailing edge geometry (main effect is on the amplitude of shedding)
- boundary layer thickness
- lock-in condition of shedding frequency (see Chapter 2.3)

As can be seen there is some ambiguity in the estimation of Strouhal number in hydraulic turbines, because: first, most of the experiments are done for cylinders; and, second, the Reynolds numbers in the experiments are usually significantly lower than the Reynolds number in a hydraulic machine. [16]

There is also ambiguity concerning the characteristic body dimension; some authors, e.g. Dörfler, take only the body “thickness” into account: In case of simple objects as a cylinder, D would be the diameter; in case of turbine blades, the trailing edge thickness is the appropriate characteristic length, as the thickness of the trailing edge determines the scale of the eddies. [7]

While other authors prefer to include also the boundary layer thickness into the body dimension definition. Then the Strouhal number (for blunt trailing edge hydrofoil) is defined as:

$$St = \frac{f_s * (h_t + 2\delta)}{C_{ref}} \quad (2.3)$$

where h_t is a hydrofoil trailing edge thickness and δ is a boundary layer thickness. [1]

In Figure 2.6 there is the relationship between Reynolds and Strouhal number for the flow past circular cylinder presented by Schlichting which indicates constant Strouhal number for some intervals of Reynolds number. $St = 0.21$ for $400 < Re < 6000$ and $St = 0.19$ for $2 \times 10^4 < Re < 10^5$.

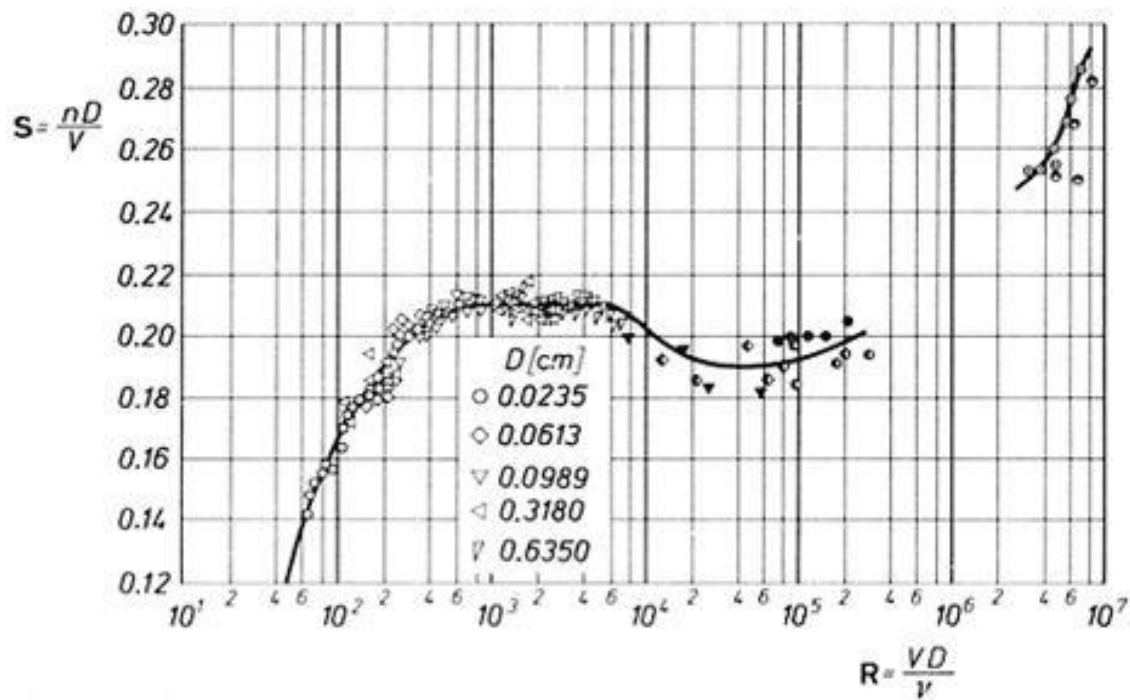


Fig. 2.6 Reynolds number – Strouhal number relationship [19]

2.3 Lock-in Condition

As mentioned above, the body placed in a flow experience a fluctuating lift force transverse to the flow caused by the asymmetric formation of vortices. This lift force may cause the vibration of the structure. The coincidence of the vortex shedding frequency with the natural frequency of the fluid-structure system over a range of velocity is referred to as a lock-in phenomenon, for the shedding frequency is “locked” onto the natural frequency of the system. The ability of the fluid-structure system to synchronize the shedding frequency with its natural frequency is one of the fundamental features of flow-induced vibration. [24]

Such a condition is usually accompanied by significant increase of noise and results in the resonant vibration of the structure, which leads to considerably high amplitudes. Since the frequency is usually high, large number of vibrational cycles is reached in relatively short time which can lead to high-cycle fatigue of the structure and eventually to its premature failure. [7] Gummer [13] says: assuming a typical natural fundamental frequency in bending of 70 Hz in water for the stay vane of a large turbine, we arrive at 2.52×10^5 cycles per hour of operation.

For the understanding of the lock-in phenomenon the Figure 2.7 (presented by Dörfler [7]) can help. It shows the behavior of frequency and amplitude (in this case the torque amplitude, however the lift amplitude behaves equally) depending on increasing flow velocity. As the velocity grows, the Strouhal number (Equation 2.2) remains constant which is represented in the diagram by straight black line. Once the vortex shedding frequency reaches the natural frequency of the structure (in this case about 300 Hz), the Strouhal number is no longer constant. For a considerably wide range of flow velocity, the shedding frequency remains “locked” onto the natural

frequency, until the difference between the shedding frequency and the natural frequency becomes too large.

As for the amplitude, the only condition with noticeable vibrations is near the resonance between vortex shedding frequency and a natural frequency of the vane. Under the lock-in condition, the amplitude is considerably higher and that is the main reason, why the lock-in condition is so dangerous in terms of fatigue life of the structure.

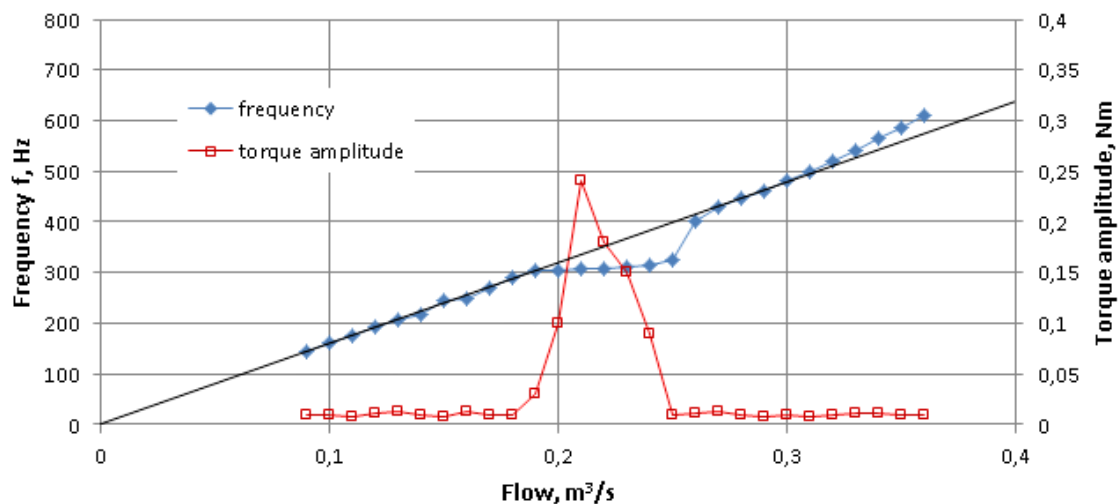


Fig. 2.7 Lock-in condition, acc.[7]

It was already mentioned that the vortex shedding induces vibration of the structure transverse to the flow and that this vibration is most apparent in case of lock-in condition. It should be mentioned, however, that each time a vortex is shed, a weak fluctuating drag is generated, and oscillations can be induced also streamwise with the fluid flow. Streamwise vibrations caused by this effect have not been observed for bodies in air, but in denser fluids such as water, where the ratio of the mass of fluid displaced to the mass of the body is substantially greater, serious oscillations can occur. However the maximal amplitudes of streamwise vibration are much smaller than those of vibration transverse to the flow and hence streamwise vibration is not so dangerous and less attention is paid to it. [7]

3 STAY VANE CRACKING

Despite the long history of stay vane cracking (one of the first reports of the incident was published in 1968 by Goldwag and Berry [12]) and profound theoretical and experimental investigation of the phenomenon, the vortex induced cracking still occurs nowadays.

In Figure 3.1 there is a cross-section of typically arranged Francis turbine unit. From this figure, it is clear how the water flows in the unit: it comes via penstock, passes the cascade of stay vanes (fixed ones that close the force loop of pressurized spiral case) and guide vanes (mobile ones that control the flow rate through the unit), transmits the power to the runner and leaves the unit via draft tube.

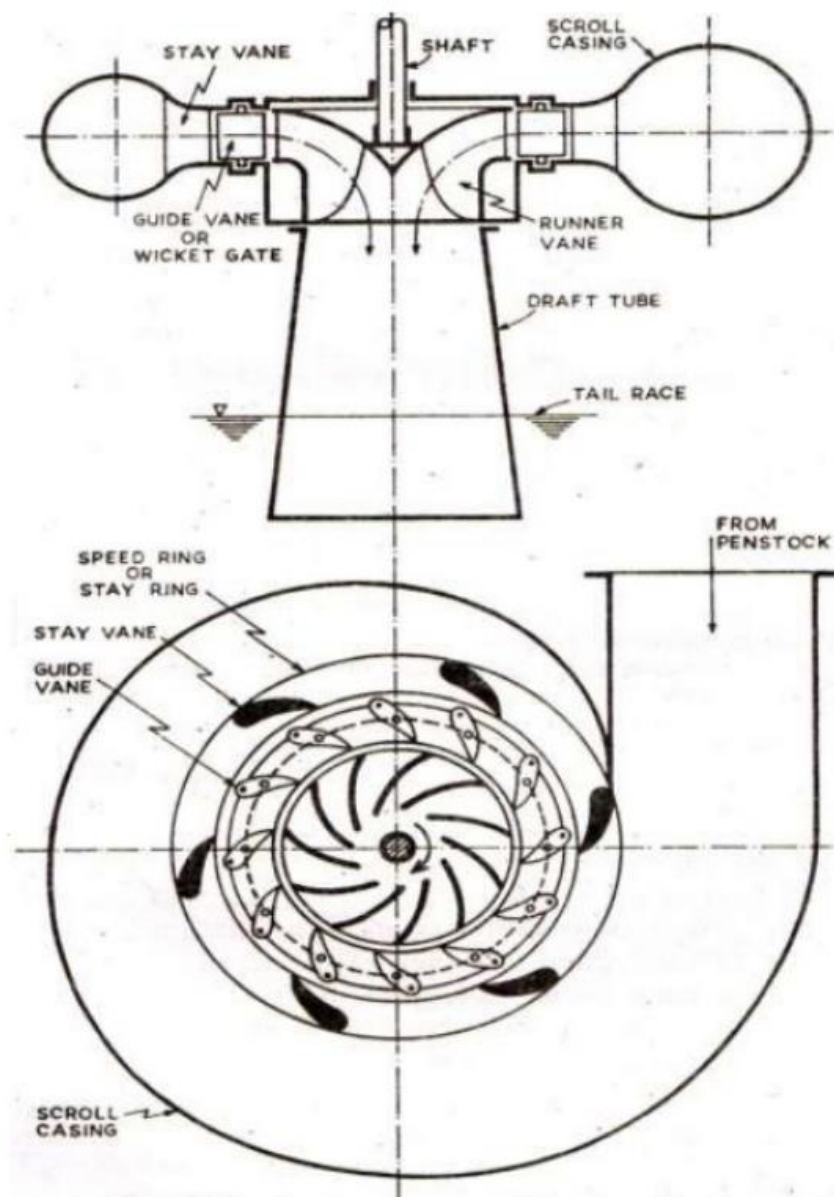


Fig. 3.1 Cross-section of Francis turbine unit [20]

The stay vanes have three basic functions:

- to act as a bracing of the spiral case
- to transmit any vertical loads from the concrete and headcover
- to direct water at the correct angle from the spiral case to the guide vanes

To meet such requirements, the stay vanes are exposed to the forces from pressurized spiral case, vertical forces from the weight of the generator and the hydraulic thrust transmitted through the concrete and headcover, and hydraulic forces caused by the water passing through the vanes. [13]

Since the spiral case with the stay ring is fixed part of the erected unit and hence any repair is difficult and expensive, it is essential to avoid any possible situation that would cause the damage. Repairs also imply the loss of generating hours which in case of large hydro-power plants is an expensive problem. Therefore the vortex induced vibration in hydraulic machines should be a subject of concern.

The actual wave of cracking caused by vortex-induced vibration started in mid-1960s when for the first time many large Francis and Kaplan turbines were built and as Brekke [5] says, one of the reasons was the weight reduction of turbine units: The traditional way of producing high head turbines was to use steel castings in the pressure carrying part like spiral casings, head cover and bottom cover. Then the turbines became very heavy requiring a labor consuming production in foundries and workshops. Because of relatively small units this design was used up to around 1960 for the pressure carrying parts. The reason for the possibility of a weight reduction to around 1/3 for the spiral casings was the improved welding technology and the introduction of high tensile stress plates with yield point of 460 MPa. The main advantage of the weight reduction was the decrease of production costs, because less man hours were needed to produce the turbines. In addition the transport costs were reduced. The draw back with the lighter turbines was that a lighter turbine gives less damping of pressure pulsations. [5]

Concerning the vanes at that time, they often were fragile profiles not much different from a flat plate with very simple trailing edges, usually rounded which is the worst possible shape from the fluid-mechanical point of view [7] [5]

The report by Goldwag and Berry [12] mentioned above discusses the specific case of stay vane cracking that occurred at the Little Long Generating Station of Ontario Hydro which is situated about 800 km north of Toronto on the Mattagami River which flows into Hudson Bay and at the time of the report delivered 500 MW of power. However, it can well serve as an example of a typical development of such situation:

Shortly after the first unit was being commissioned and operated under load, abnormally high level of noise and vibration on the generator stator, the relay floor and the tailrace deck were reported to be present. Similar situation repeated when the second unit came into service. About six months after commissioning, the units were drained and the detailed inspection indicated that the stay vanes contained numerous and serious fatigue cracks. The diagnosis indicated the damage to be the result of von Kármán vortices. [12]

Gummer [13] remarks in his review that in most cases there was noise and vibration with the turbine operating at loads above approximately 70 % guide vane opening. Sometimes the operation was not possible above certain output, in other cases, however, neither noise nor vibration was high enough (or it was obscured by other noises and therefore overlooked) to consider any further investigation. In such cases the turbine went into operation, but the inspection after only a short operating period (about 2000 h) revealed cracks in the welds securing the vanes to the stay ring.

In most cases the damage was clearly due to fatigue caused by resonance. The cracks typically originated at or close to the welds at both ends of the trailing edge. Some crack originated also from the leading edge and some of these joined with the cracks from the trailing edge and so penetrated through the whole vane. The cracks of the stay vanes are illustrated in Figure 3.2a. [12] [13]

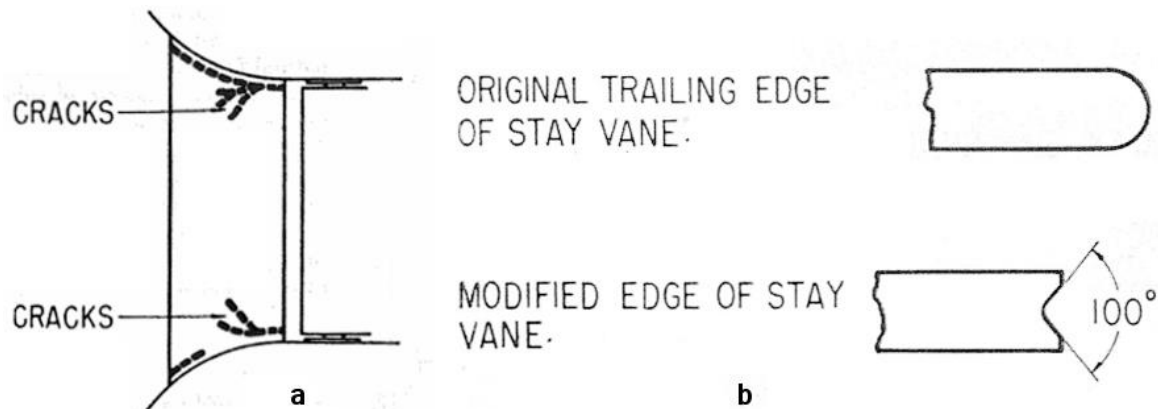


Fig. 3.2 Little Long Generating Station: a – sketch of stay vane cracks;
b – modification of stay vane trailing edge [12]

It is well known (see e.g. [16] [18]) that the trailing edge geometry has a strong influence on the amplitude of the vane oscillation and that rounded trailing edge is the worst shape from the fluid-mechanical point of view. Such trailing edges were used at Little Long Generating Station and as mentioned above, it did not work well. The trailing edge was reshaped into a “dove tail” form which considerably reduced the vibration (see Figure 3.2b). According to Dörfler [7], however, the solution was not absolutely faultless and in following years additional modifications had to be done.

Nowadays, the “dove tail” shape is usually no longer used; it is replaced by asymmetric trailing edges. One of the common shapes is an oblique cut of the blunt trailing edge with the angle of 30° . Such an edge causes that the vortices do not shed symmetrically and therefore the upper and lower vortices are not in perfect anti-phase and partly eliminate each other. The disorganization of von Kármán vortex street leads to vibration and fluctuating lift reduction. [18] [25]

Various authors (see e.g. [16] [13] or [7]) agree upon the way how to avoid the problem of resonant vibration. There are basically two principles:

- modification of the trailing edge
- altering of the natural frequency of the stay vanes

The former was already mentioned above; the latter can be done either by slotting the vane longitudinally, replacing the vane by stiffer one, or by dividing the stay vane channel in two by installing damping plates in the middle plane of the spiral casing. The plates de-tune the structure, especially of the vibration in the torsional mode, so that no further resonance occurs. [16]

Considering the complexity of these two approaches, the trailing edge modification is always the “first choice” method and only after it proves insufficient, the damping plates are installed or other steps are taken.

This thesis in the next part discusses the CFD prediction of the suitable trailing edge shape for the reduction of stay vane resonant oscillation.

II CFD SIMULATIONS

Some forty seven years ago, Goldwag and Berry [12] wrote: “The prediction of the likelihood of hydroelastic resonance by calculation has not yet been realized, and only a qualitative approach appears possible. In the case of a water turbine stay ring or runner blade, no amount of calculations would allow prediction of the critical frequencies with any certainty”. [12]

This part of the thesis should prove their statement to be no longer valid; it consists of two test cases (for suitable CFD solver setting) and the assignment provided by ČBE which is solved in accordance with the test cases. Both the test cases and the ČBE assignment were spatially discretized by means of Gambit 2.4.6 and only structured grids were used since they should provide better convergence and higher accuracy than the unstructured ones. The computation was carried out in ANSYS Fluent 15.0. The shedding frequency was in both test cases and the ČBE assignment obtained from the monitoring of y-velocity in a specific point behind the body. The time-varying monitor values served to identify the shedding frequency by means of Fast Fourier Transform algorithm (FFT).

Since the nature of the turbulence is three-dimensional, the attempt was to carry out the simulations three-dimensionally. From the results it will be apparent, however, that it did not show any considerable improvement in the accuracy of frequency values. Moreover, the 3D solution was much more time-consuming. The 2D solution was usually obtained in the order of hours, while the 3D solution computational time was in the order of days.

Von Kármán vortex street needs the transitional approach, however the unsteady calculation requires a steady state solution as initial condition. After switching to unsteady calculation mode, the solution can take a large number of time steps before the fully developed unsteady shedding phenomenon begins. So in all cases it was proceeded as follows: 2 000 iterations were computed as a steady state and after switching to unsteady state at least 10 000 time steps were computed. In some cases even after 10 000 time steps the vortex shedding was not fully developed and therefore more time steps were added to the computation.

4 FLOW PAST SQUARE CYLINDER

This case should serve as a test case for finding the optimal setting of CFD solver that would later be used for the solution of the ČBE problem. The computational results are compared with the experimental data recorded by Lyn during an experiment performed in 1992. Detailed description of Lyn's experiment can be obtained via ERCOFTAC database under the title "Vortex Shedding Past Square Cylinder". [17]

4.1 Experiment by Lyn

The experiment was performed on a square cylinder with side length $d = 40$ mm in a closed water channel supplied by a constant-head tank. At the measurement station, the channel had a 39×56 cm cross-section. A reference velocity in the channel was $c_{ref} = 0.535$ m/s. This is estimated to be within 2-3 % of the average cross-sectional velocity. The Reynolds number, based on c_{ref} and D was $Re = 21400$. The shedding frequency, f , was determined as 1.77 ± 0.05 Hz. This estimate agreed within experimental error with an estimate based on spectral analysis of the raw pressure signal. The resulting Strouhal number was $St = f D / c_{ref} = 0.132 \pm 0.004$.

A two-colour LDV forward-scatter system measured two components of instantaneous point velocities. A reference phase was defined from a low-pass-filtered pressure signal taken from a tap at the midpoint of cylinder sidewall. The time of occurrence of an LDV velocity realization was marked in relation to the pressure signal, permitting the association of the velocity data with a particular phase of the vortex shedding cycle. All velocity realizations occurring within the same phase bin or interval constituted an ensemble at constant phase, such that statistic at constant phase could be evaluated.

Measurements were confined to the upper half of the flow region in order to reduce the number of measurements needed. It was assumed that the flow in the lower half could be obtained by reflecting the measured upper flow about the centerline. [17]

4.2 CFD Simulation of flow past Square Cylinder

The simulation of transient flow past square cylinder was performed in two- and three-dimensional spatial discretization. For both 2D and 3D simulation two computational models were used: the realizable k- ϵ model and the Reynolds Stress model (RSM).

Both k- ϵ model and RSM are primarily valid for turbulent core flows (i.e., the flow in the regions somewhat far from walls). Therefore it should be considered how to make these models suitable for wall-bounded flows.

Traditionally, there are two approaches to modeling the near-wall region. In one approach, the viscosity-affected inner region is not resolved. Instead, semi-empirical formulas called "wall functions" are used to bridge the viscosity-affected region between the wall and the fully-turbulent region. The usage of wall functions prevents the need to modify the turbulence models to account for the presence of the wall.

In another approach, the turbulence models are modified to enable the viscosity-affected region to be resolved with a mesh all the way to the wall, including the viscous sublayer. For purposes of discussion, this will be termed the "near-wall modeling" approach. These two approaches are depicted schematically in Figure 4.1. [9]

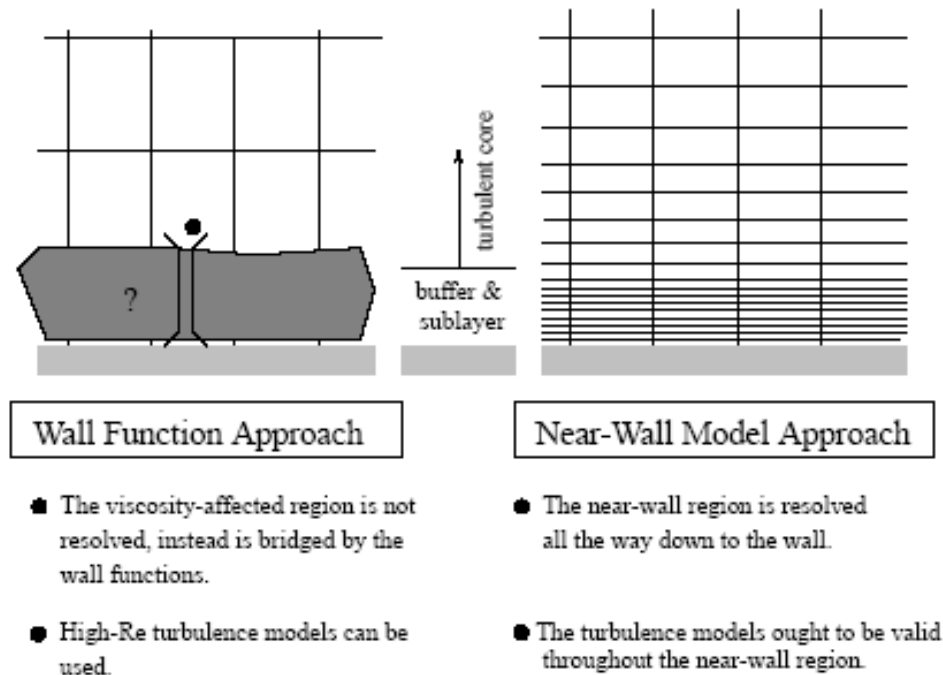


Fig. 4.1 Two approaches to near-wall region treatment [9]

In most high-Reynolds-number flows, the wall function approach substantially saves computational resources, because the viscosity-affected near-wall region, in which the solution variables change most rapidly, does not need to be resolved. The wall function approach is popular because it is economical, robust, and reasonably accurate. It is a practical option for the near-wall treatments for industrial flow simulations. [9]

There are basically two types of wall functions: Standard wall functions and non-equilibrium wall functions. The latter are recommended for use in complex flows involving separation, reattachment, and impingement where the mean flow and turbulence are subjected to severe pressure gradients and change rapidly. Therefore when modeling von Kármán vortex street, the non-equilibrium wall functions are suitable.

4.2.1 2D Simulation

Spatial discretization:

The origin of the coordinate system of the computational domain is located in the center of the cylinder, and all distances are non-dimensionalized by d (side length of the cylinder $d = 40$ mm). Inlet is placed $10.d$ in front of the cylinder, while outlet is $20.d$ behind the cylinder. The width of the computational domain is $14.d$ (i.e. 560 mm) which corresponds with the experiment. Dimensions and boundary conditions of the computational domain are depicted in Figure 4.2.

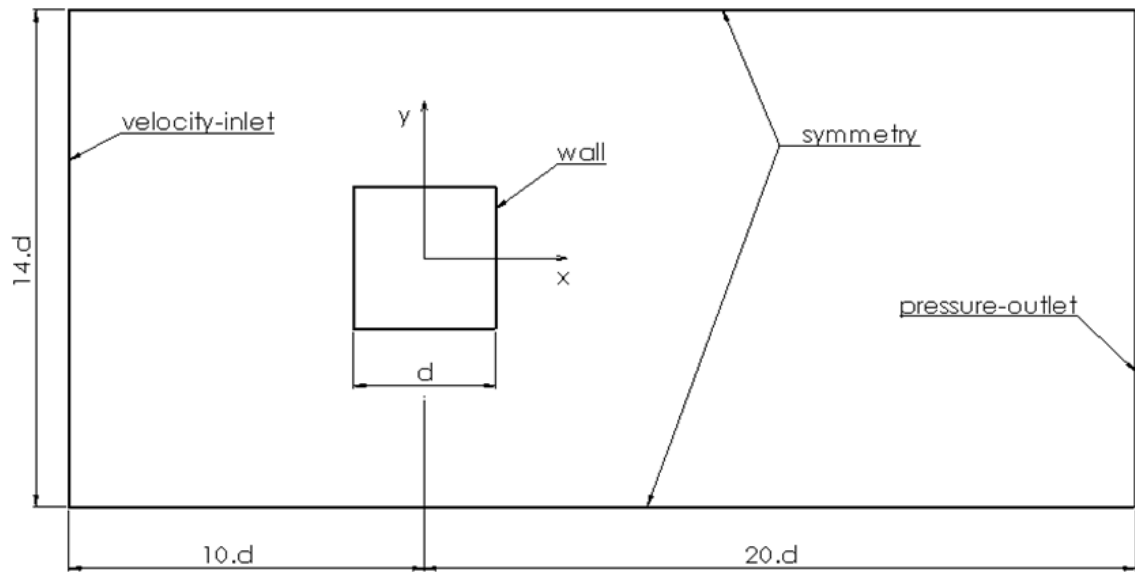


Fig. 4.2 Sketch of the computational domain, acc. [22]

For proper description of the vorticity, the computational mesh should be dense near the cylinder walls. The actual mesh and its detail near the cylinder wall are in Figure 4.3 and Figure 4.4 respectively.

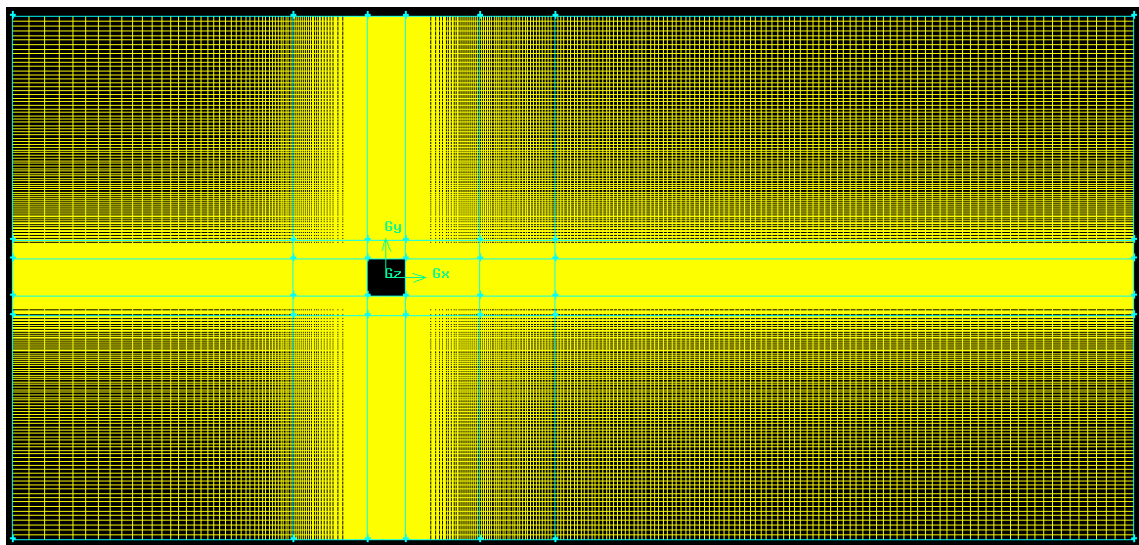


Fig. 4.3 Spatial discretization of the domain

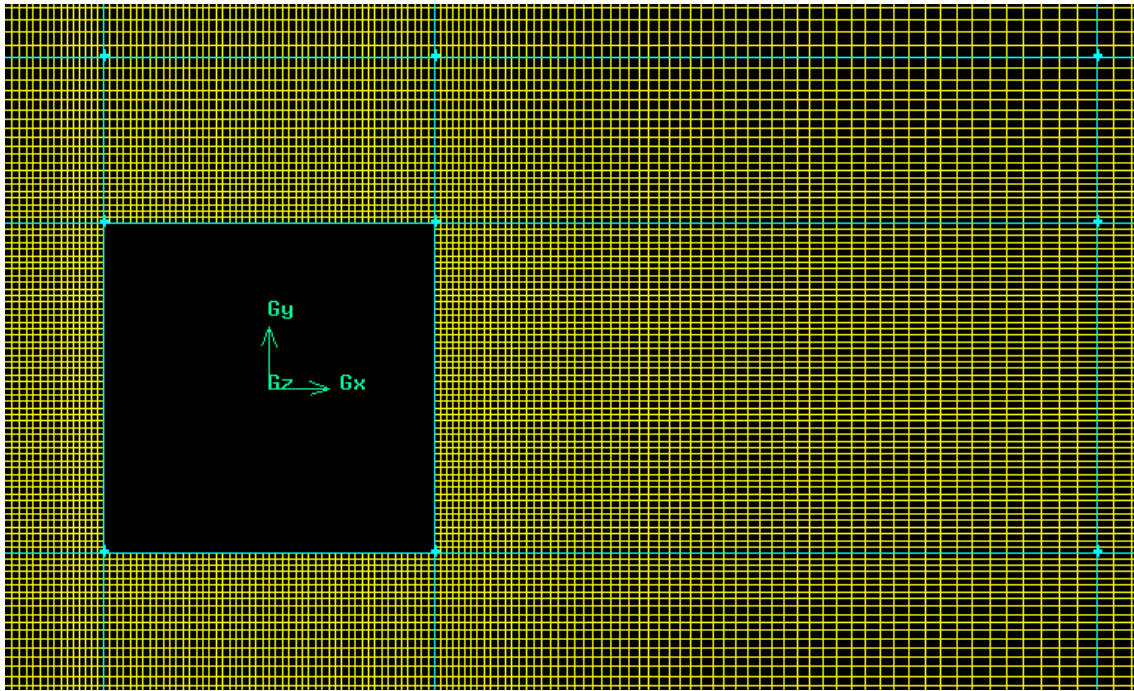


Fig. 4.4 Detail of the mesh near the cylinder walls

The mesh consists of 82 500 quadrilateral cells; the Map meshing type that creates a regular, structured grid of mesh elements is used. Maximum Aspect ratio (ratio of longest to the shortest side in a cell) is 24.881, however such a high ratio could only be found at both inlet and outlet area; values of ratio around the cylinder walls range between 1 and 7.

Solver setting:

Boundary conditions are based on Lyn's experiment.

On the velocity-inlet bc the velocity magnitude is $c_{ref} = 0.535$ m/s, turbulent intensity 5 % and hydraulic diameter $D = 0.04$ m. (Hydraulic diameter is the size of the biggest possible vortex, which in this case corresponds with the cylinder side length.)

On the pressure-outlet bc the gauge pressure is $p = 0$ Pa, turbulent intensity 10 % and hydraulic diameter $D = 0.04$ m.

Sides of the computational domain are defined as symmetry bc which means there is no friction and the normal velocity $c_n = 0$ m/s.

Sides of the square cylinder are defined as wall bc.

In the first case, the realizable k- ϵ model was used as a turbulence model together with the non-equilibrium wall functions.

Solution methods:

Gradient – Least Squares Cells Based

Pressure – Standard

Momentum – QUICK

Turbulent Kinetic Energy k – Second Order Upwind

Turbulent Dissipation rate ϵ – Second Order Upwind

Discretization of the unsteady term – Second Order Implicit

In the second case the Reynolds Stress model (RSM) was used as a turbulence model together with the non-equilibrium wall functions.

Solution methods:

Gradient – Least Squares Cells Based

Pressure – Standard

Momentum – QUICK

Turbulent Kinetic Energy k – Second Order Upwind

Turbulent Dissipation rate ε – Second Order Upwind

Reynolds Stresses – Second Order Upwind

Discretization of the unsteady term – Second Order Implicit

For both cases the time step was $\Delta t = 0.00565$ s.

4.2.2 3D Simulation

Spatial discretization:

To the existing geometry the third dimension was added in the extent of 50 mm. The three-dimensional mesh consists of 550 000 hexahedral cells. Maximum Aspect ratio is 11.726. The computational mesh for 3D simulation is depicted in Figure 4.5, where the boundary conditions are also indicated by colors: blue means velocity-inlet, red is pressure outlet, yellow is symmetry (on the front surface of the domain the symmetry bc is not depicted for higher clearness) and white is wall bc.

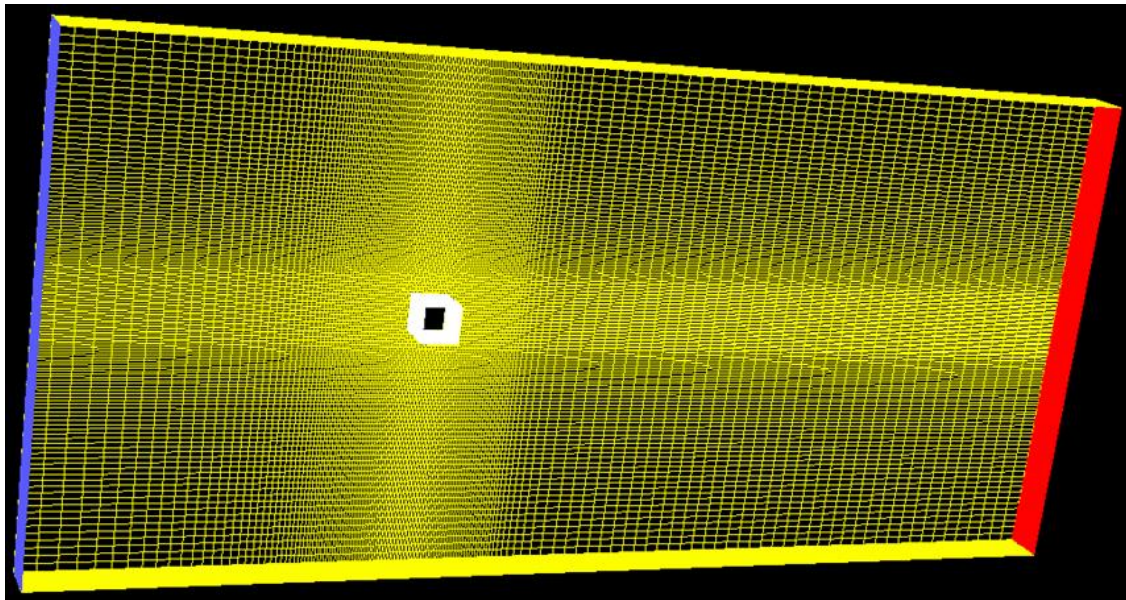


Fig. 4.5 3D mesh with boundary conditions color indication

Wall y^+ values:

y^+ is a dimensionless distance from the wall for wall-bounded flow and its value limits the usage of wall functions. It is defined as follows:

$$y^+ = \frac{u_\tau^* y}{\nu} \quad (4.1)$$

where y is the distance to the nearest wall, ν is the local kinematic viscosity of the fluid and u_τ is friction velocity at the nearest wall defined as:

$$u_\tau = \sqrt{\frac{\tau_w}{\rho}} \quad (4.2)$$

where τ_w is a wall shear stress and ρ is the fluid density. [9]

The recommended value of y^+ for the use of wall functions (i.e. for both realizable $k-\varepsilon$ and RSM models) lies between 20 and 120. The distribution of wall y^+ values for 3D flow past square cylinder is depicted in Figure 4.6.

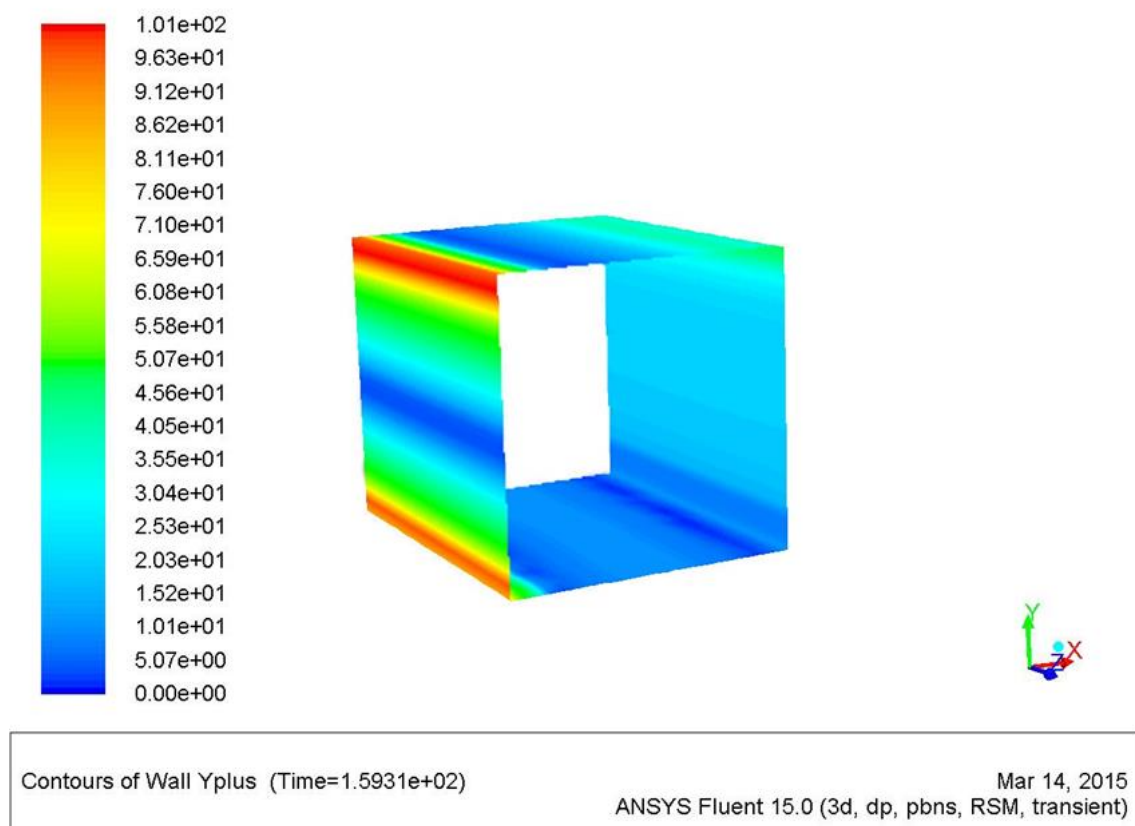


Fig. 4.6 Distribution of wall y^+ values

The setting of the solver was identical with the 2D approach and equally so the solution methods and the time step.

4.3 CFD Results

The y-velocity was monitored in the point downstream of the square cylinder with the coordinates $x, y, z = [0.15; 0; 0]$ m. The obtained values of shedding frequency for individual models and approaches are presented in Table 4.1; the contours of static pressures are presented in Figures 4.7 to 4.10 and the contours of vorticities are presented in Figures 4.10 to 4.14. The difference presented in Table 4.1 refers to Lyn's value 1.77 Hz, the experimental error (± 0.05 Hz) is not taken into account.

	k-ϵ	dif.	RSM	dif.
	Hz	%	Hz	%
2D	1.89	6.78	1.93	9.04
3D	1.85	4.52	1.97	11.30

Tab. 4.1 Computed values of shedding frequency

From the table 4.1 it is apparent that realizable k- ϵ model is slightly more accurate than the Reynolds Stress model; although in the absolute value of the frequency the difference is not so profound, when the percentage is taken into consideration, the difference is more significant, particularly in 3D approach. The comparison between 2D and 3D simulation for both realizable k- ϵ model and RSM does not show any relevant differences. From the figures below it can be seen that the RSM predicts higher turbulence in the flow past square cylinder.

On the basis of these results it is decided that for the second test case (Flow past NACA 0009 Hydrofoil, Chapter 5) primarily the realizable k- ϵ model will be used.

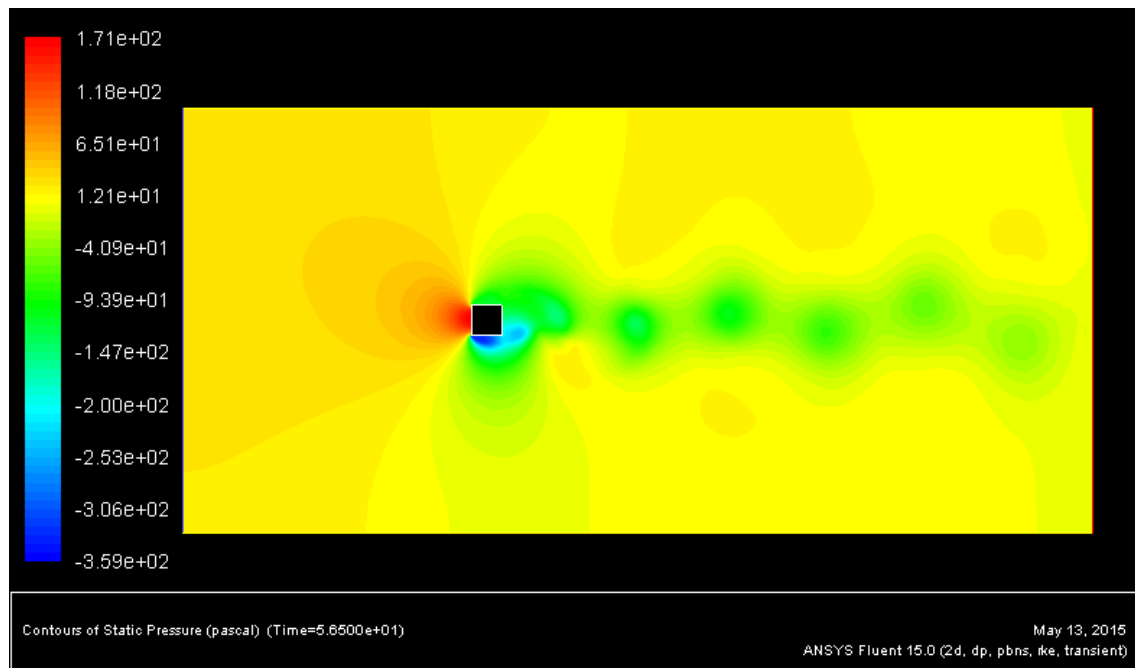


Fig. 4.7 Contours of static pressure for 2D realizable k-ε

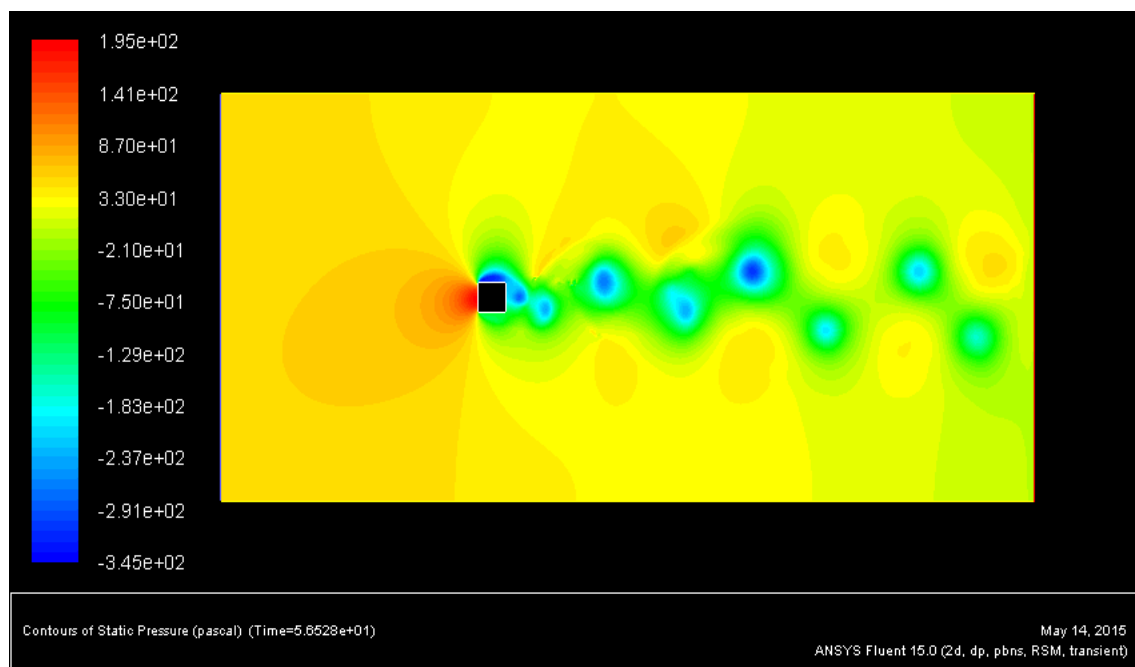


Fig. 4.8 Contours of static pressure for 2D RSM

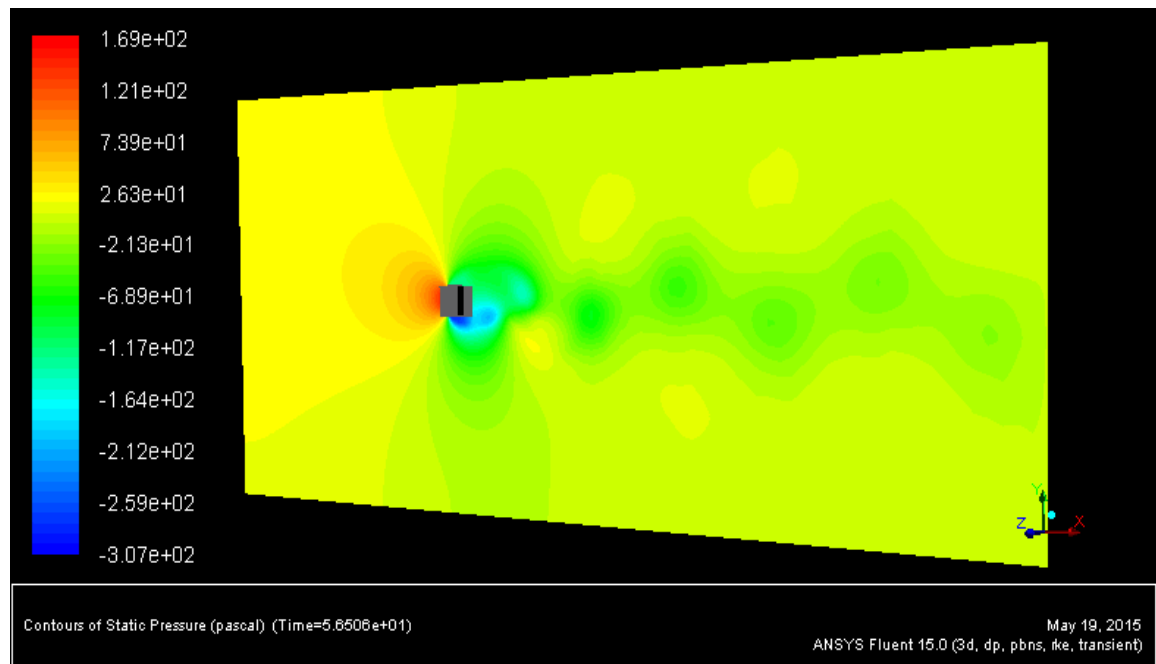


Fig. 4.9 Contours of static pressure for 3D realizable k- ϵ

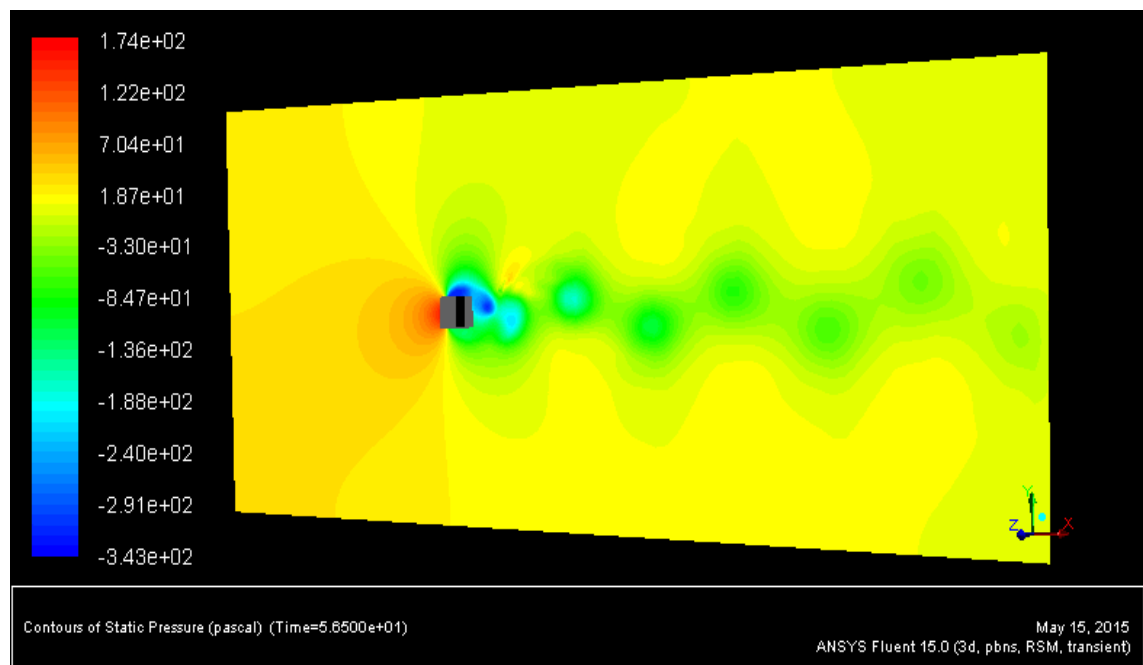


Fig. 4.10 Contours of static pressure for 3D RSM

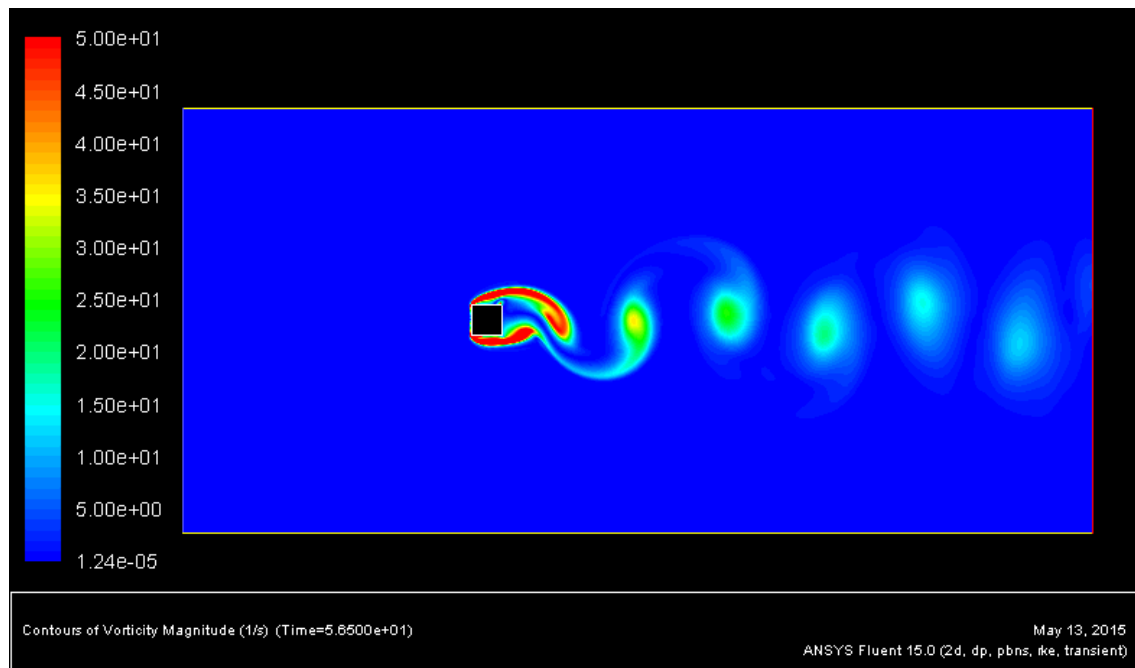


Fig. 4.11 Contours of vorticity for 2D realizable $k-\epsilon$

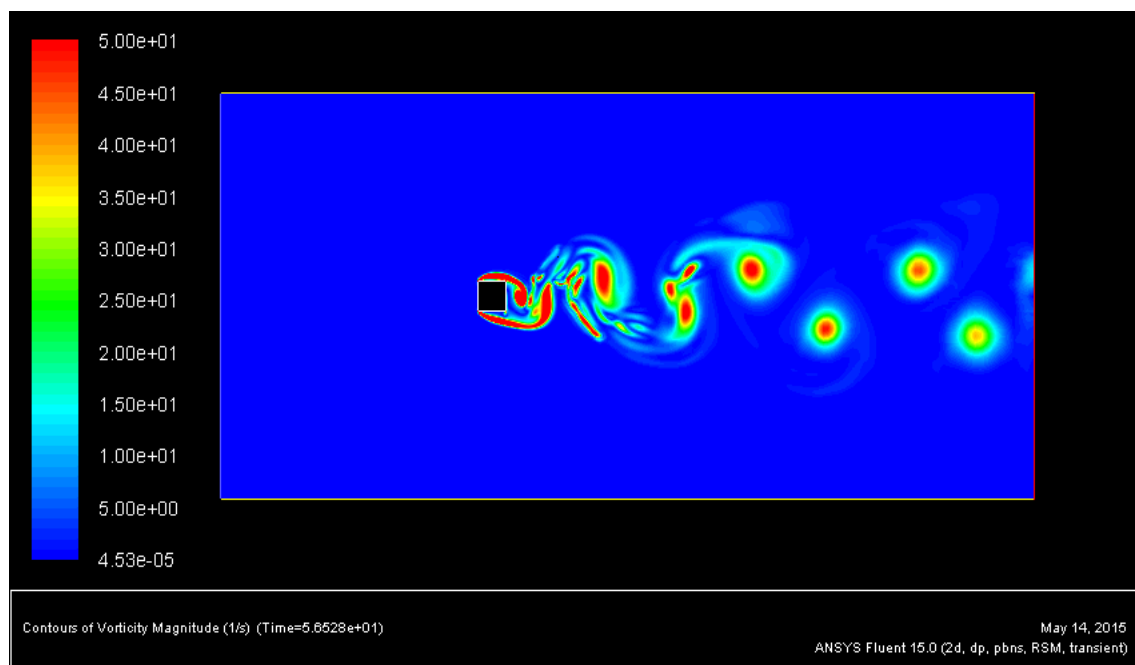


Fig. 4.12 Contours of vorticity for 2D RSM

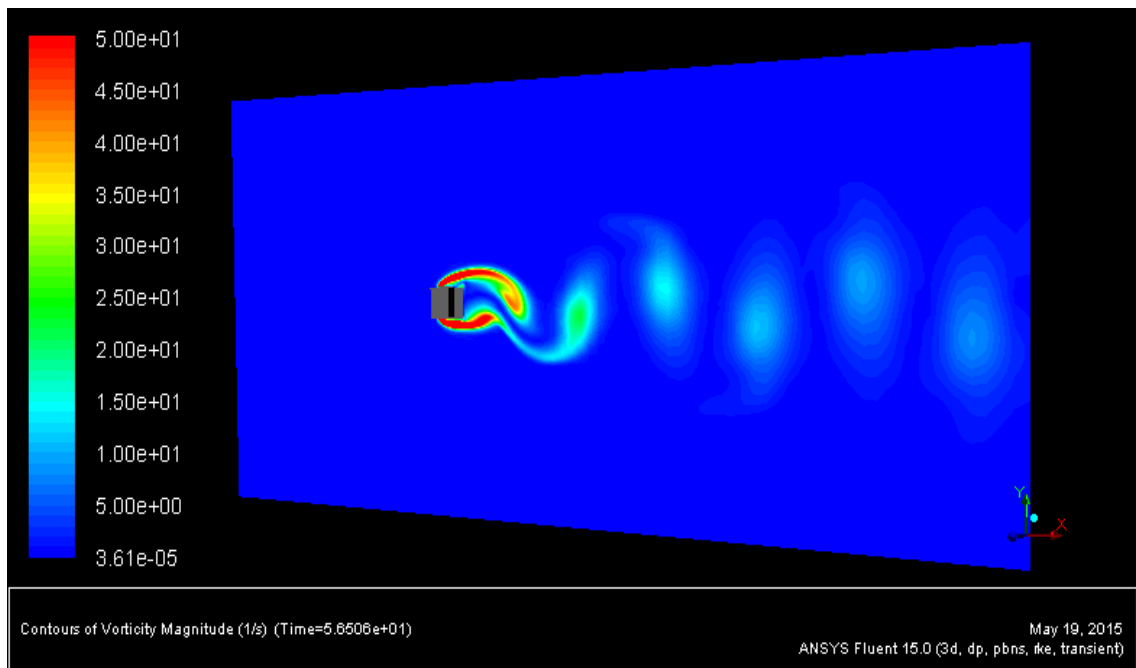


Fig. 4.13 Contours of vorticity for 3D realizable $k-\epsilon$

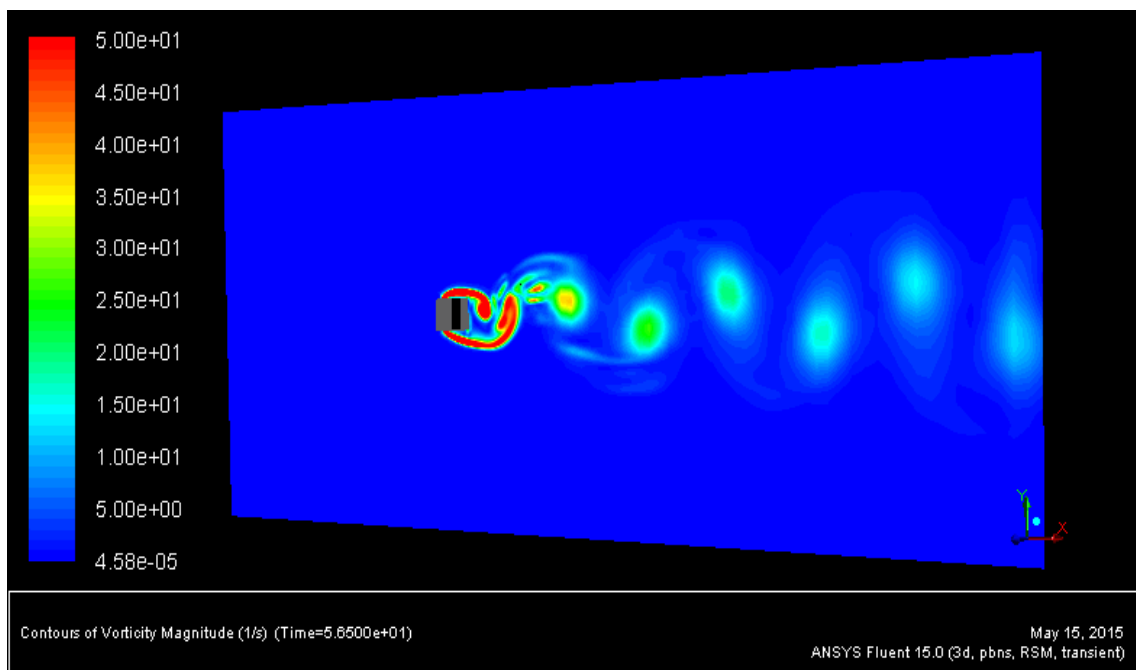


Fig. 4.14 Contours of vorticity for 3D RSM

5 FLOW PAST NACA 0009 HYDROFOIL

The second test case should verify the ability of the solver to respond to the hydrofoil trailing edge modification. The computation results are confronted with the experimental data assembled and presented in 2012 by Zobeiri in his PhD. thesis at École Polytechnique Fédérale De Lausanne (EPFL) in Switzerland. [24]

5.1 Experiment by Zobeiri

5.1.1 Test Rig

The measurements were performed in the EPFL high-speed cavitation tunnel, with a test section of 150 x 150 x 750mm; maximum inlet velocity, $c_{max} = 50$ m/s, and maximum static pressure, $p_{ref} = 16$ bar. The high-speed cavitation tunnel is depicted in Figure 5.1. A nozzle with reduction in area 46 to 1 is used to obtain a uniform velocity distribution in the test section. A long diffuser, installed downstream of the test section, is used to recover the dynamic pressure by reducing the flow velocity to 3% of its value at the test section inlet. The bubble trap section collects bubbles in the flow. They tend to rise due to the buoyancy effect until they reach one of the plates and then are convected along the plate. The double suction pump provides a total head of 36.5 m for the flow rate of 1.125 m³/s at 885 rpm and it is directly driven by a 500 KW power DC-electric motor. A constant air pressure is kept over the free surface in the pressure vessel to control the pressure. [24]

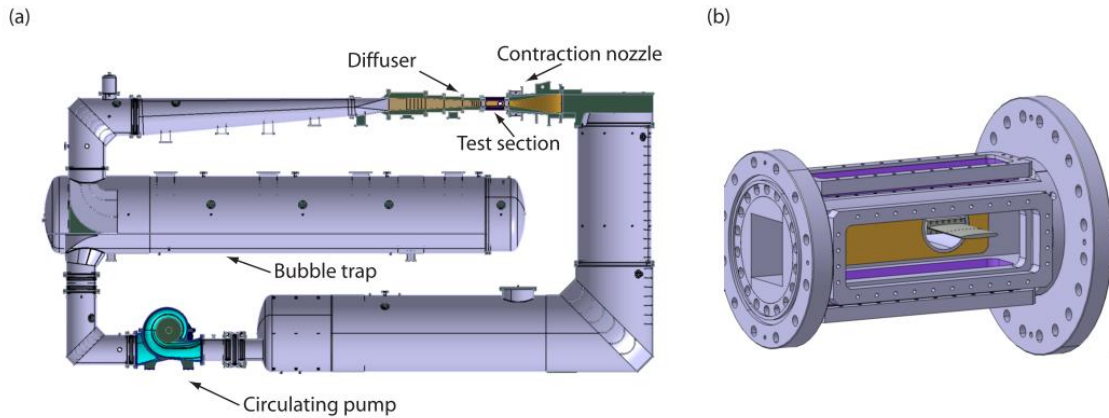


Fig. 5.1 EPFL high speed cavitation tunnel: a – whole rig, b – test section [24]

5.1.2 Experimental Hydrofoil

The tested hydrofoil is based on *NACA 0009-7.845/1.93* with the maximum thickness equal to 9% of the chord length. The hydrofoil is made of stainless steel with chord and span lengths of 110 mm and 150 mm respectively. As a reference hydrofoil *NACA 0009* blunt truncated at $L = 100$ mm with trailing edge thickness of 3.22 mm is selected. The reference hydrofoil is presented in Figure 5.2. The geometry is defined in x ; y ; z coordinate system with the origin placed at the hydrofoil leading edge.

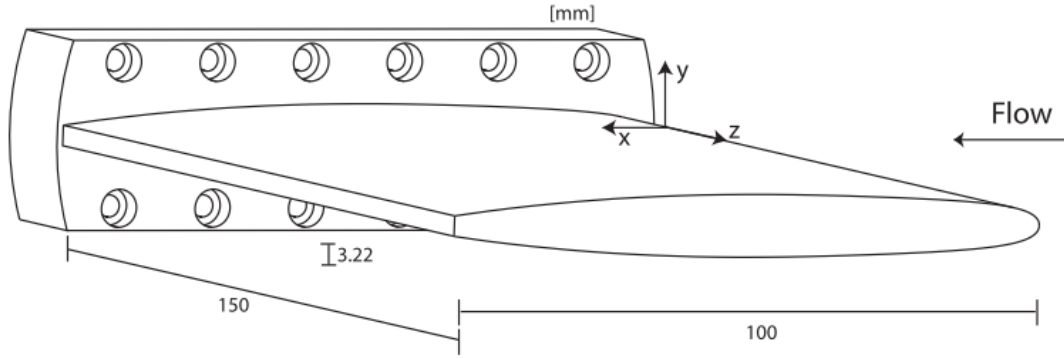


Fig. 5.2 Reference hydrofoil NACA 0009 blunt truncated [24]

The curve of the hydrofoil is defined by following equations:

$$0 \leq \frac{x}{L_0} \leq 0.5 \quad \frac{y}{L_0} = a_0 \left(\frac{x}{L_0} \right)^{\frac{1}{2}} + a_1 \left(\frac{x}{L_0} \right) + a_2 \left(\frac{x}{L_0} \right)^2 + a_3 \left(\frac{x}{L_0} \right)^3$$

$$0.5 \leq \frac{x}{L_0} \leq 1 \quad \frac{y}{L_0} = b_0 + b_1 \left(1 - \frac{x}{L_0} \right) + b_2 \left(1 - \frac{x}{L_0} \right)^2 + b_3 \left(\frac{x}{L_0} \right)^3$$

where L_0 is the original chord length and

$a_0 = + 0.1737$	$b_0 = + 0.0004$
$a_1 = - 0.2422$	$b_1 = + 0.1737$
$a_2 = + 0.3046$	$b_2 = - 0.1898$
$a_3 = - 0.2657$	$b_3 = + 0.0387$

The test case hydrofoils are based on reference hydrofoil *NACA 0009*. The only difference is the modified trailing edges. The first case study is an oblique trailing edge hydrofoil with the trailing edge cut at about 93% of the chord length at an angle of 30° . Its trailing edge thickness is quarter of blunt trailing edge thickness. The second case study is a Donaldson trailing edge hydrofoil. This hydrofoil is shaped by modifying the blunt trailing edge with a combination of a straight line with an angle of 45° and a 3rd polynomial curve. All three hydrofoil trailing edges are depicted in figure 5.3.

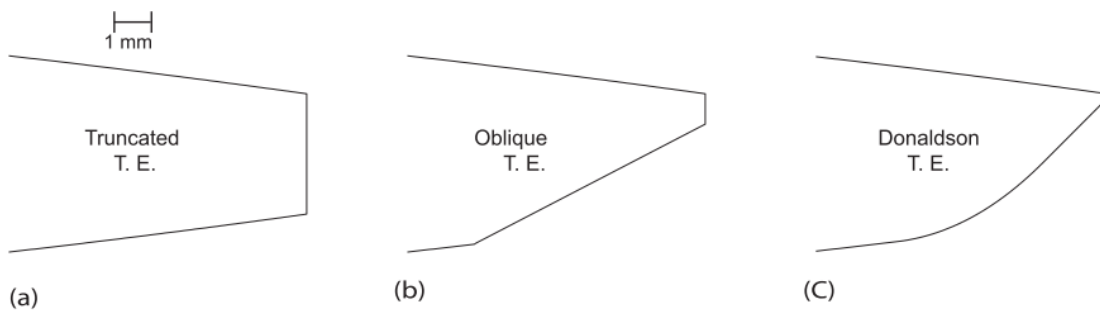


Fig. 5.3 NACA 0009 hydrofoil trailing edges: a – truncated, b – oblique, c – Donaldson [24]

5.1.3 Experiment Results

Zobeiri measured the shedding frequency for two modes of the boundary layer for each hydrofoil: the hydrofoils are made from stainless steel and polished to mean surface roughness, $Ra = 0.15 \mu\text{m}$. The hydrofoil surface is therefore considered to be hydraulically smooth over the entire experimented free-stream velocity range. A natural turbulent transition can occur beyond a certain distance from the leading edge. So called tripped transition is artificially reached by means of a distributed roughness made of glue and $125\mu\text{m}$ diameter sand placed on both sides of the hydrofoil, 4mm downstream from the stagnation line and 4 mm wide, Figure 5.4. The glue and sand combination create a $150 \mu\text{m}$ high, two-dimensional flow obstacle while the sand strip itself provides multiple three dimensional protuberances. Hence forth, this configuration is designated as the tripped transition. In contrast, the case without rough strips is designated as the natural transition. [1]

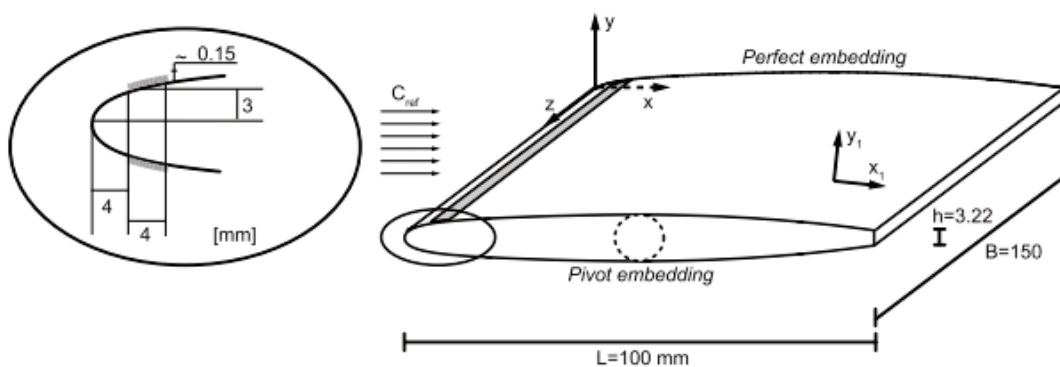


Fig. 5.4 Distributed roughness on the leading edge [1]

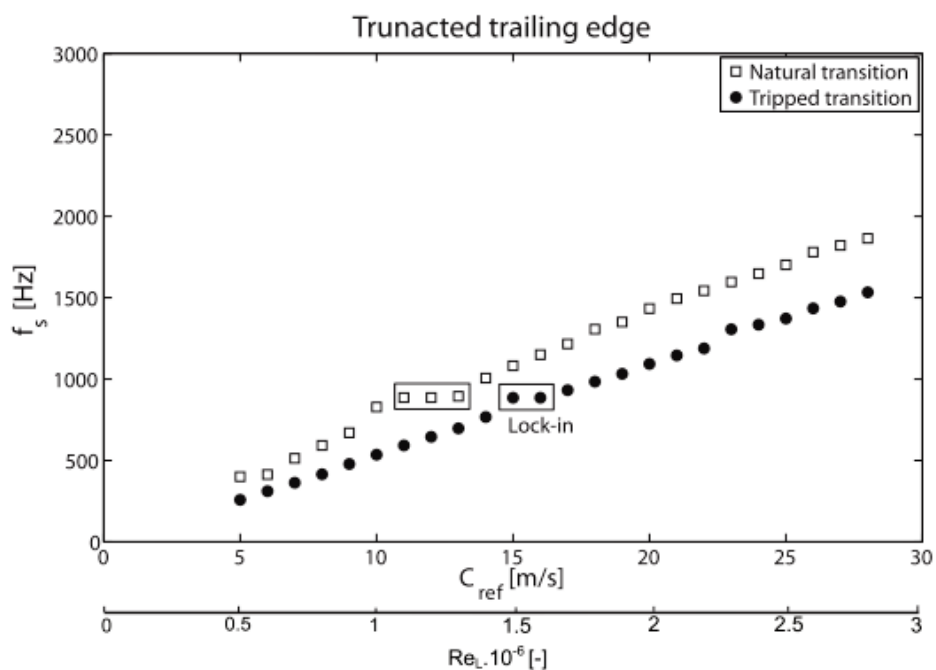


Fig. 5.5 Shedding frequency values for truncated trailing edge [1]

The measured values for truncated, oblique and Donaldson trailing edges are recorded in diagrams in Figure 5.5, 5.6 and 5.7 respectively. The Reynolds number values in these figures are based on the boundary layer thickness.

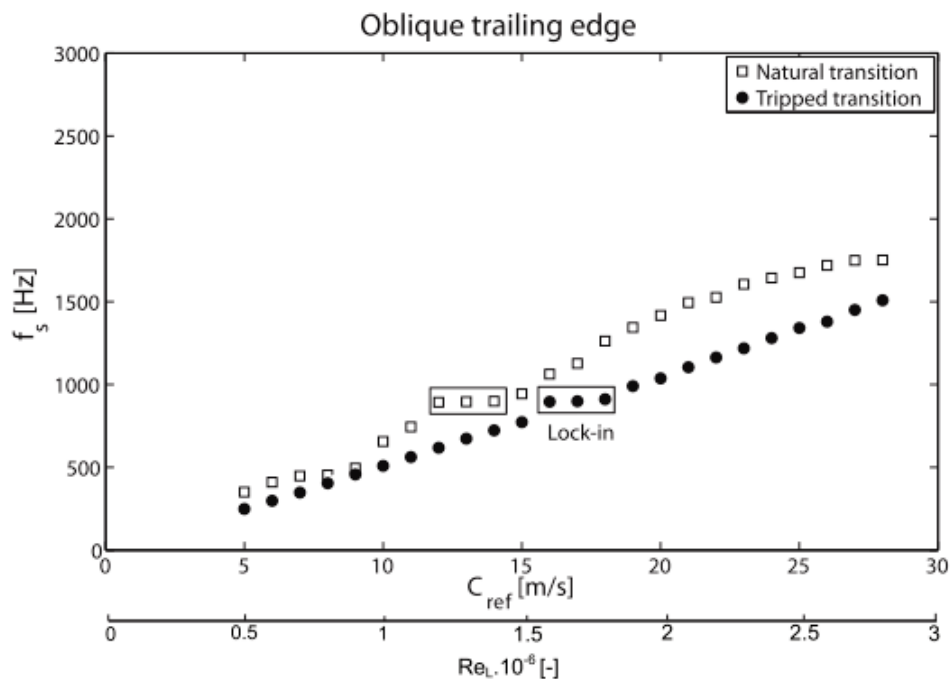


Fig. 5.6 Shedding frequency values for oblique trailing edge [1]

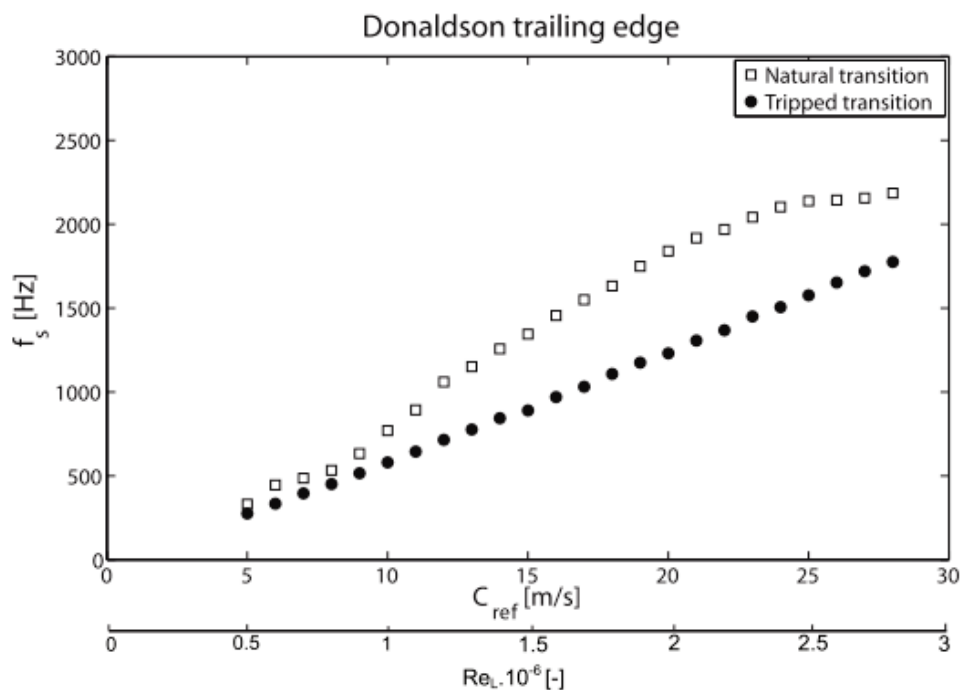


Fig. 5.7 Shedding frequency values for Donaldson trailing edge [1]

5.2 CFD Simulation of flow past NACA 0009 Hydrofoil

The simulation is based on data assembled by Zobeiri: since the CFD simulation predicts the boundary layer as fully turbulent, it is compared with the data recorded for the tripped transition mode. And since it is unable to cover the lock-in phenomenon [16], five values of velocity were chosen (7, 13, 20, 22 and 28 m/s) that do not lie in the region affected by the lock-in. For the reference hydrofoil (with blunt truncated trailing edge) the computations were carried out using realizable k - ϵ model both in 2D and 3D to verify the conclusion from the previous test case. Besides realizable k - ϵ model the SST k - ω model (shear stress transition) was used in 2D for the comparison of the results. The other two hydrofoils (oblique and Donaldson) were computed only by 2D realizable k - ϵ model.

5.2.1 2D Simulation

Spatial discretization:

The origin of the coordinate system of the computational domain is located at the leading edge of the hydrofoil. The inlet is placed 220 mm in front of the hydrofoil. The domain is 150 x 750 mm which corresponds to the dimensions of the test section of EPFL test rig. The sketch of the domain with labeled boundary conditions is presented in Figure 5.8.

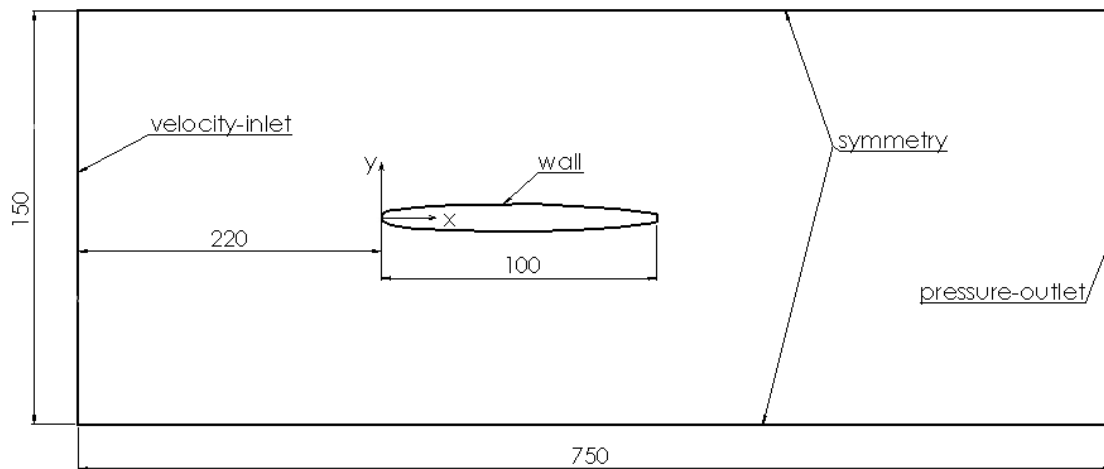


Fig. 5.8 Sketch of the computational domain

In the first case, the realizable k - ϵ model was used as a turbulence model together with the non-equilibrium wall functions. For this case the spatial discretization of the reference hydrofoil domain and the details of all three trailing edges are in Figure 5.9 and 5.10 respectively. All the meshes consist of 36 758 quadrilateral cells; the Map meshing type is used. The attempt was to make all the meshes as identical as possible so that the results could be subsequently compared.

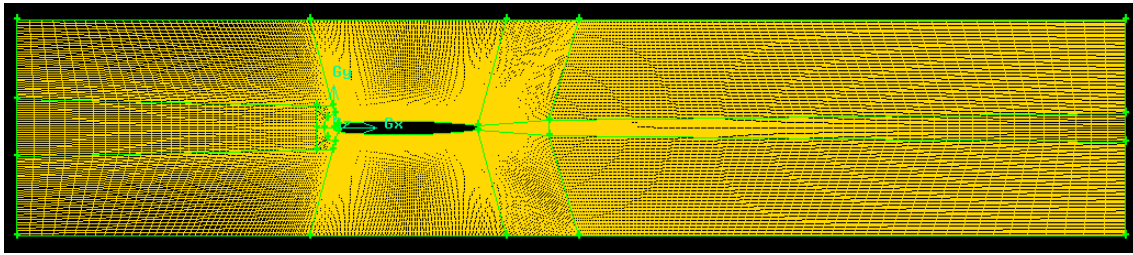


Fig. 5.9 Spatial discretization of the domain

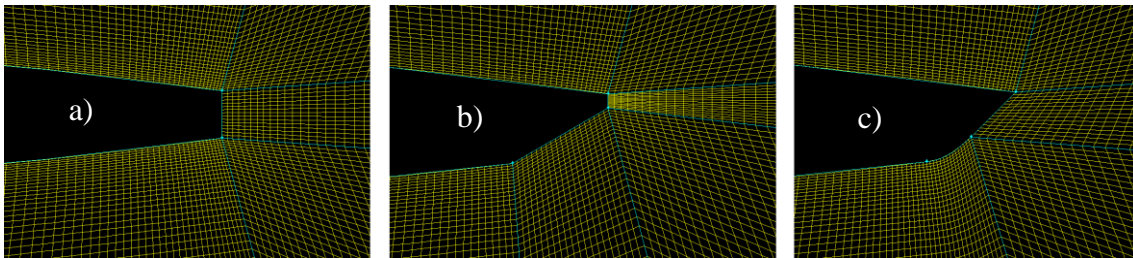


Fig. 5.10 Detail of trailing edges: a – truncated; b – oblique; c - Donaldson

Solver setting:

Boundary conditions are based on Zobeiri's experiment.

On velocity-inlet bc the velocity magnitude is successively $c_{ref} = 7, 13, 20, 22$ and 28 m/s, turbulent intensity 5% and hydraulic diameter $D = 0.01$ m, based on maximal hydrofoil thickness.

On pressure-outlet bc the gauge pressure is $p = 0$ Pa, turbulent intensity 10% and hydraulic diameter $D = 0.01$ m.

Sides of the computational domain are defined as symmetry bc which means there is no friction and the normal velocity $c_n = 0$ m/s.

The hydrofoil is defined as wall bc.

Solution methods:

Gradient – Least Squares Cells Based

Pressure – Standard

Momentum – QUICK

Turbulent Kinetic Energy k – Second Order Upwind

Turbulent Dissipation rate ε – Second Order Upwind

Discretization of the unsteady term – Second Order Implicit

In the second case the SST k - ω model was used as a turbulence model. For this case the spatial discretization of the domain differs from the first case, because SST k - ω model was designed to be applied throughout the boundary layer (i.e. does not use the wall functions) and so the mesh had to be considerably denser. For the models that do not use wall functions the recommended value of y^+ is around 1. [9] Therefore the mesh consists of 432 960 quadrilateral cells; again the Map meshing type is used. Such a density of the mesh causes noticeably longer computational time. The distribution of y^+ value along the hydrofoil is in Figure 5.11.

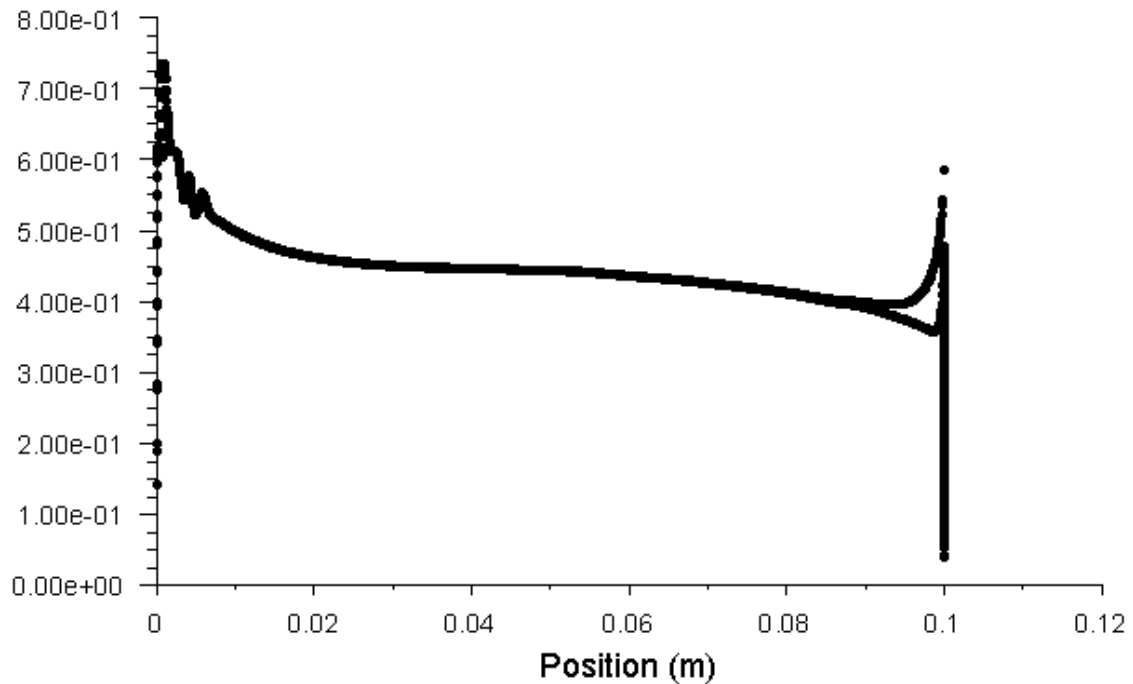


Fig. 5.11 Distribution of y^+ values along the hydrofoil

Solution methods:

Gradient – Least Squares Cells Based
 Pressure – Standard
 Momentum – QUICK
 Turbulent Kinetic Energy k – Second Order Upwind
 Turbulent Dissipation rate ε – Second Order Upwind
 Reynolds Stresses – Second Order Upwind
 Discretization of the unsteady term – Second Order Implicit

For both cases the time step was $\Delta t = 5e-6$ s.

5.2.2 3D Simulation

Spatial discretization:

To the existing 2D mesh for k - ε model the third dimension was added in the extent of 150 mm so that the computational domain corresponds with the test section of the EPFL test rig. The mesh consists of 2 205 480 hexahedral cells; the Map meshing type is used.

The setting of the solver was identical with the 2D approach and equally so the solution methods and the time step.

5.3 CFD Results

The y-velocity was monitored in the point downstream of the hydrofoil with the coordinates $x, y, z = [0.12; 0; 0]$ m. In addition to the y-velocity, the lift coefficient was monitored to determine the lift force affecting the hydrofoil. The Reynolds number values in the following tables (for all three hydrofoils) are based on the free stream velocity and the maximum hydrofoil thickness $t_{max} = 10$ mm.

At first, let us deal with the reference (blunt truncated) hydrofoil and the impact of different solution approaches on the results. The obtained values of shedding frequency for 2D and 3D realizable k- ϵ and 2D SST k- ω models are presented in Table 5.1 and Figure 5.12.

Truncated								
c_{ref}	Re	experiment	2D k- ϵ	dif.	SST k- ω	dif.	3D k- ϵ	dif.
m/s	-	Hz	Hz	%	Hz	%	Hz	%
7	69665.0	357	385	7.8	397	11.2	366	2.5
13	129377.9	689	747	8.4	794	15.2	758	10.0
20	199042.9	1097	1175	7.1	1224	11.6	1154	5.2
22	218947.2	1184	1303	10.1	1282	8.3	1282	8.3
28	278660.0	1531	1666	8.8			1671	9.1

Tab 5.1 Values of shedding frequency for truncated trailing edge

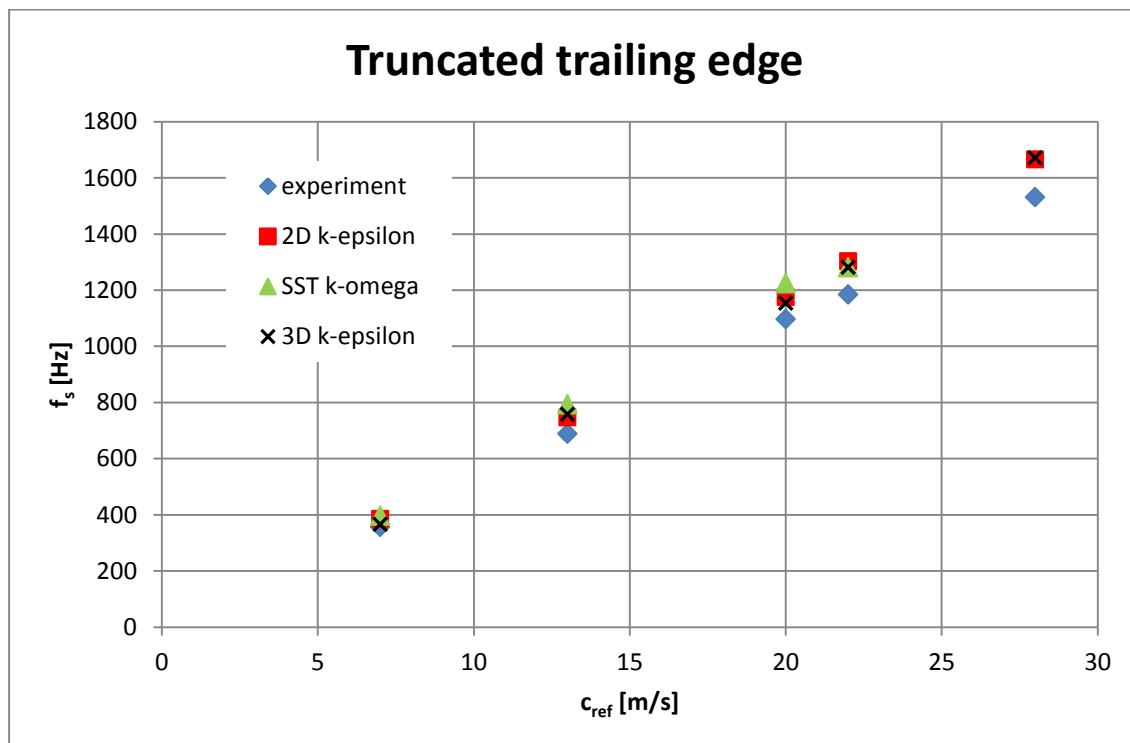


Fig. 5.12 Velocity dependent shedding frequency values for truncated trailing edge

From the presented results of the shedding frequency it can be seen that neither the denser mesh nor the 3D approach to the problem provides significantly more accurate results. Strictly speaking the vortex shedding phenomenon is three dimensional and the CFD solver is able to predict this fact (see Figure 5.13 where the “deformation” of the vortices in the third dimension is visible); however, when the computational time is taken into consideration, it is clear that the wall functions 2D approach is sufficiently accurate, robust and economical. Both 3D realizable $k-\varepsilon$ and 2D SST $k-\omega$ models need the computational time in the order of days, whereas 2D realizable $k-\varepsilon$ is able to provide reasonable results in the order of hours. The contours of vorticity for the individual approaches are presented in Figures 5.14 to 5.16.

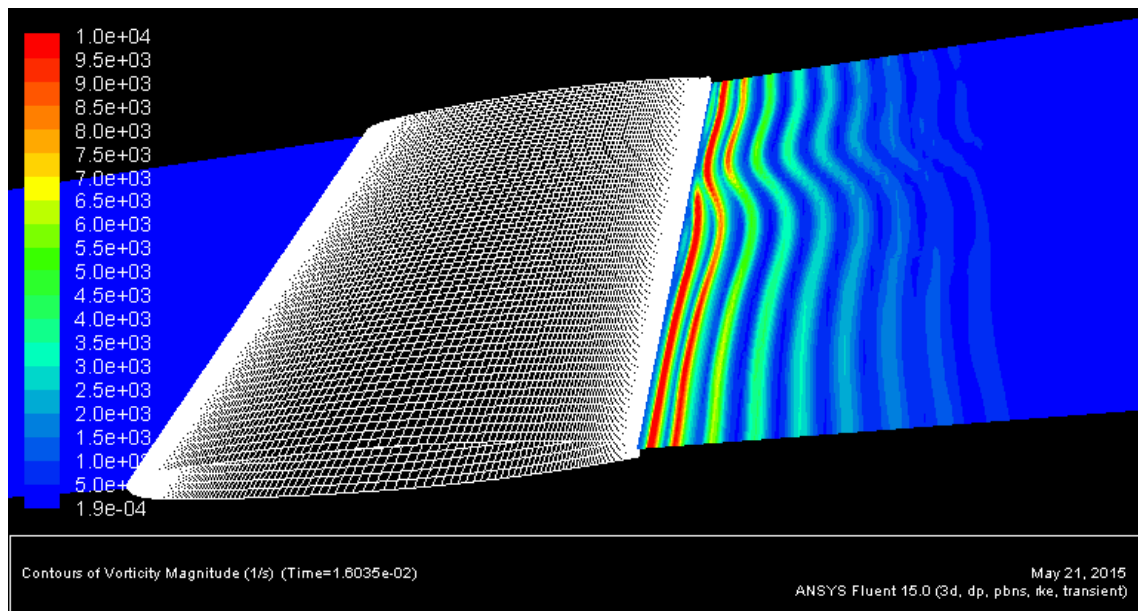


Fig. 5.13 3D nature of the vorticity

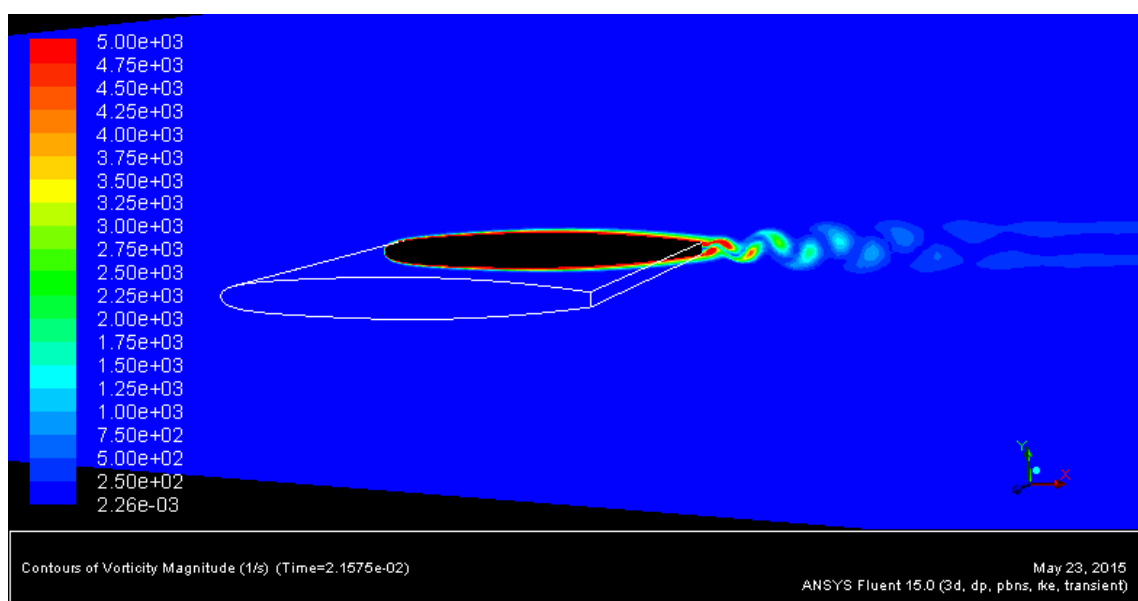


Fig. 5.14 Contours of vorticity, 3D realizable $k-\varepsilon$

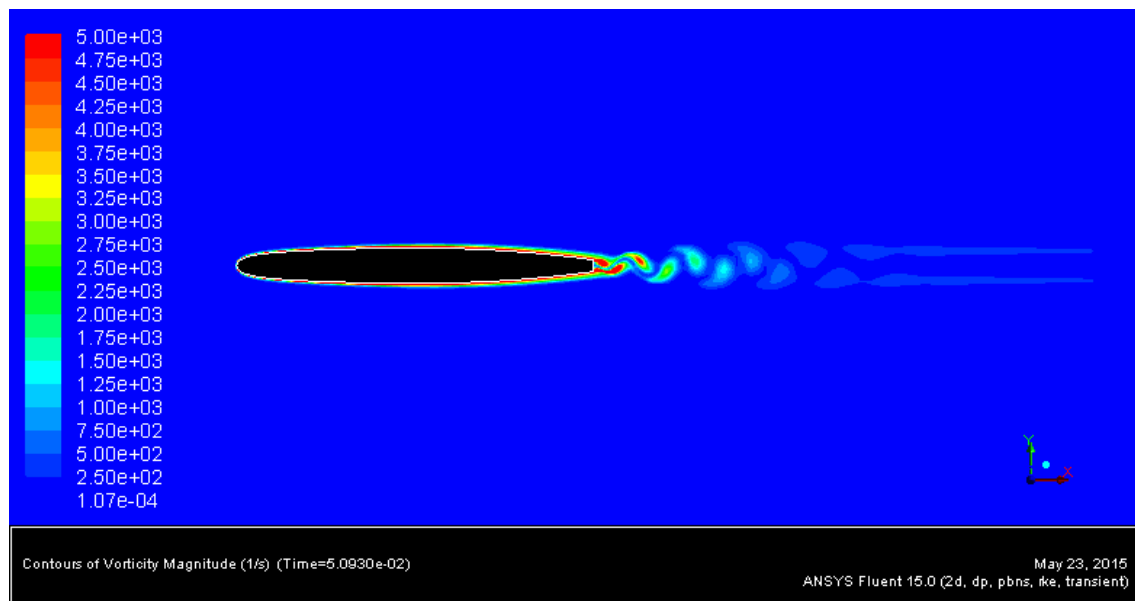


Fig. 5.15 Contours of vorticity, 2D realizable k- ϵ

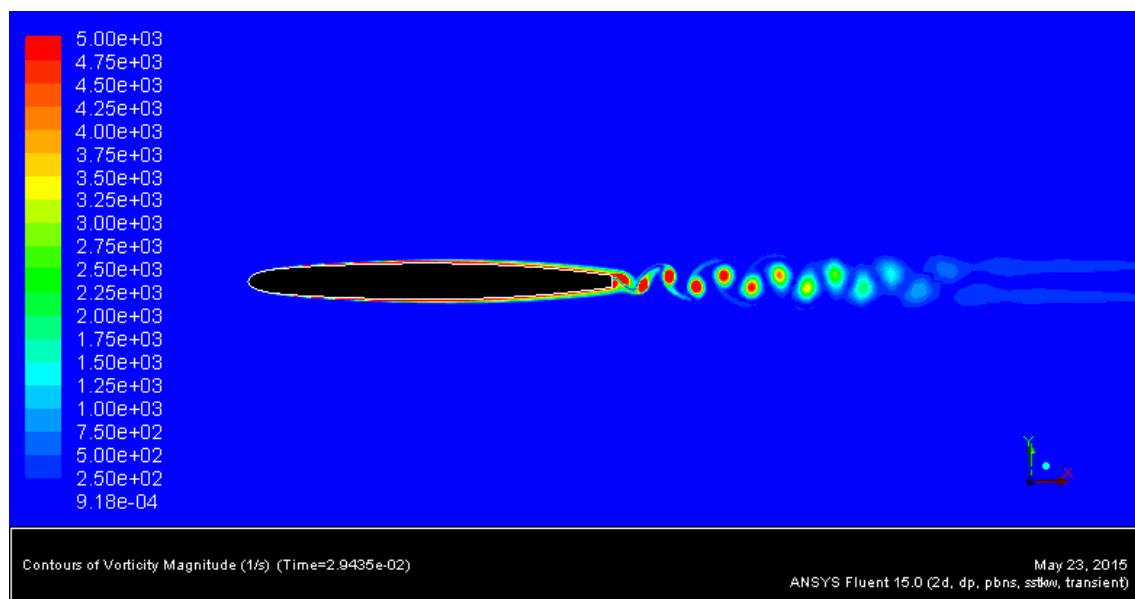


Fig. 5.16 Contours of vorticity, 2D SST k- ω

From the figures above, it is apparent that concerning the vorticity, there is no considerable difference between 2D and 3D k- ϵ models; however the SST k- ω model predicts significantly stronger vorticity.

The values of the lift force affecting the trailing edge for individual approaches are presented in Figure 5.17. The values were obtained from the amplitude of the lift coefficient which is defined as:

$$C_L = \frac{F_L}{\frac{1}{2} \rho c_{ref}^2 A} \quad (5.1)$$

where F_L is the lift force, ρ is the fluid density, c_{ref} is the free stream velocity and A is the area of the hydrofoil. [9]

The results of the lift force values show a significant difference between individual approaches. This corresponds with Dörfler [7] and other authors who claim that the shedding frequency prediction is neither significantly dependent on the grid, nor strongly influenced by the choice of the turbulence model, whereas the prediction of the amplitude strongly depends on both.

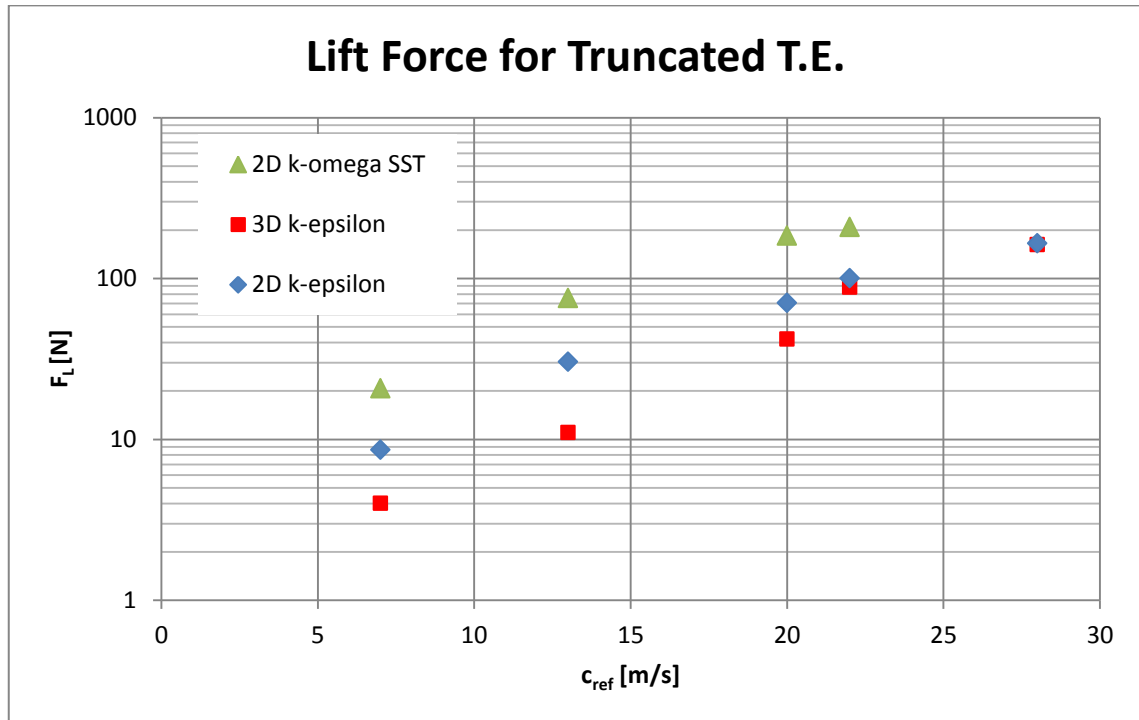


Fig. 5.17 Velocity dependent lift force amplitude for truncated trailing edge

Unfortunately it is not possible to verify which of the approaches predicts the lift force amplitude more exactly because in Zobeiri's experiment only the vibrational amplitude was observed. Although the absolute value of the lift force is not known, the qualitative comparison of the hydrofoils with different trailing edges is possible.

Due to the time-efficiency, the comparison of the individual hydrofoils is based on 2D realizable k- ϵ model computation.

The obtained data for the oblique trailing edge are presented in Table 5.2 and in Figure 5.18. Compared with the truncated trailing edge, the CFD results of this case considerably differ from the experimental results. Whereas for the truncated trailing edge the difference from the experiment was around 10 %, this case reveals the difference around 40 %. The question is whether the experimental data are correct; the data assembled by Zobeiri show the decrease in the shedding frequency for the oblique trailing edge, various articles, however (see e.g. [18], [13]), show on the contrary the increase of the shedding frequency with which correspond the CFD results.

Oblique				
c_{ref}	Re	experiment	2D k-ε	dif.
m/s	-	Hz	Hz	%
7	69665.0	337	491	45.7
13	129377.9	667	949	42.3
20	199042.9	1026	1457	42.0
22	218947.2	1154	1603	38.9
28	278660.0	1500	2073	38.2

Tab. 5.2 Values of shedding frequency for oblique trailing edge

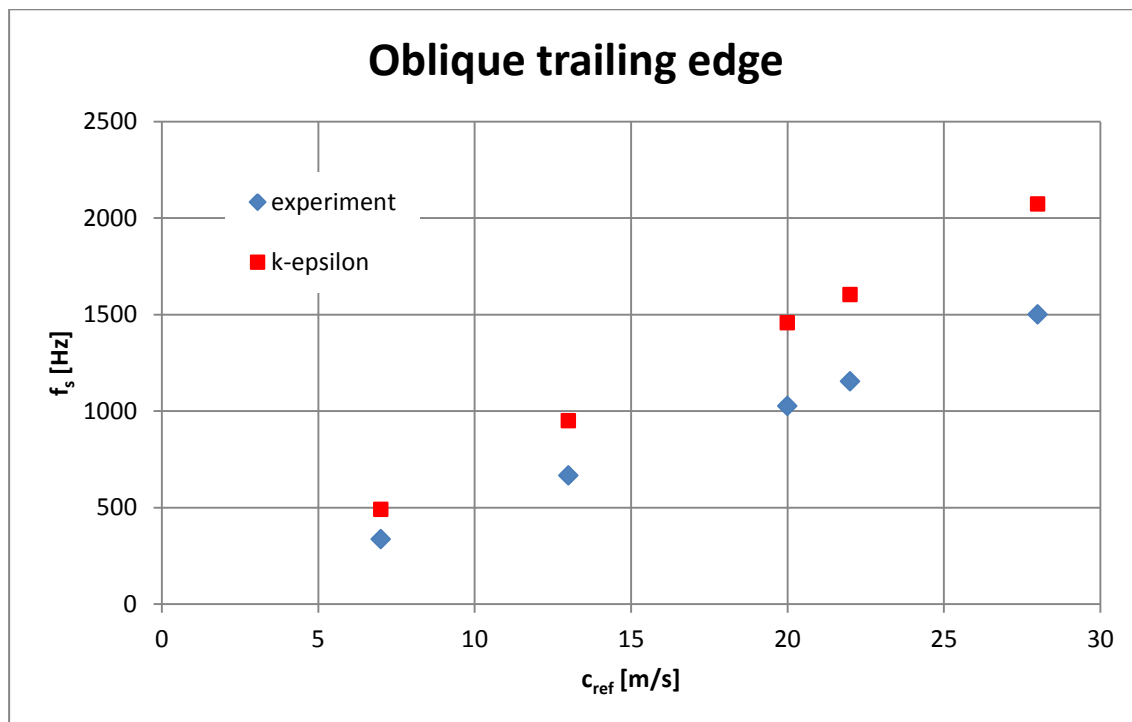


Fig. 5.18 Velocity dependent shedding frequency for oblique trailing edge

The CFD results for the Donaldson trailing edge are presented in Table 5.3 and in Figure 5.19. Concerning the difference from the experiment, this case is similar to the truncated trailing edge: it shows the difference of about 10 % from the experiment.

Donaldson				
c_{ref}	Re	experiment	2D k- ϵ	dif.
m/s	-	Hz	Hz	%
7	69665.0	395	437	10.6
13	129377.9	781	859	10.0
20	199042.9	1234	1351	9.5
22	218947.2	1367	1489	8.9
28	278660.0	1784	1923	7.8

Tab. 5.3 Values of shedding frequency for Donaldson trailing edge

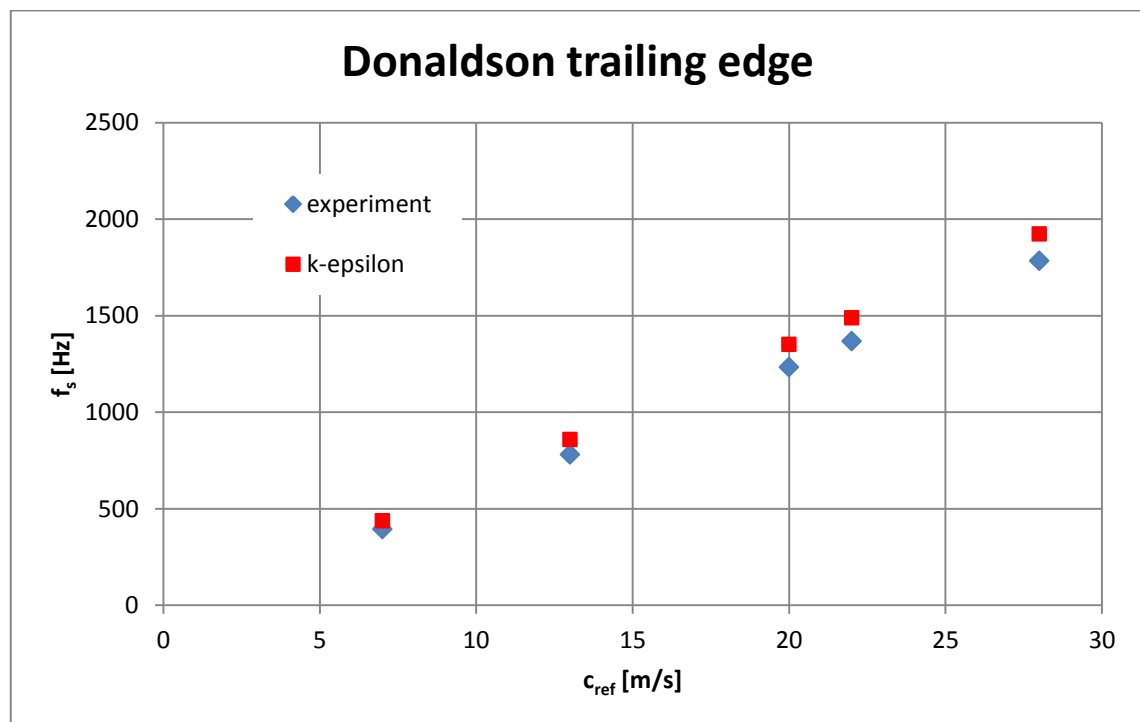


Fig. 5.19 Velocity dependent shedding frequency for Donaldson trailing edge

The comparison of CFD results for shedding frequencies of all three hydrofoils as a function of free stream velocity is presented in Table 5.4 and in Figure 5.20. It shows the increase of the frequency for both oblique and Donaldson trailing edges as compared to the reference hydrofoil. The Figure 5.20 shows quasi-linear relationship between the shedding frequency and the free stream velocity in all three cases.

c_{ref}	Re	truncated	oblique	Donaldson
m/s	-	Hz	Hz	Hz
7	69665.0	385	491	437
13	129377.9	747	949	859
20	199042.9	1175	1457	1351
22	218947.2	1303	1603	1489
28	278660.0	1666	2073	1923

Tab. 5.4 Values of shedding frequency for truncated, oblique and Donaldson trailing edges

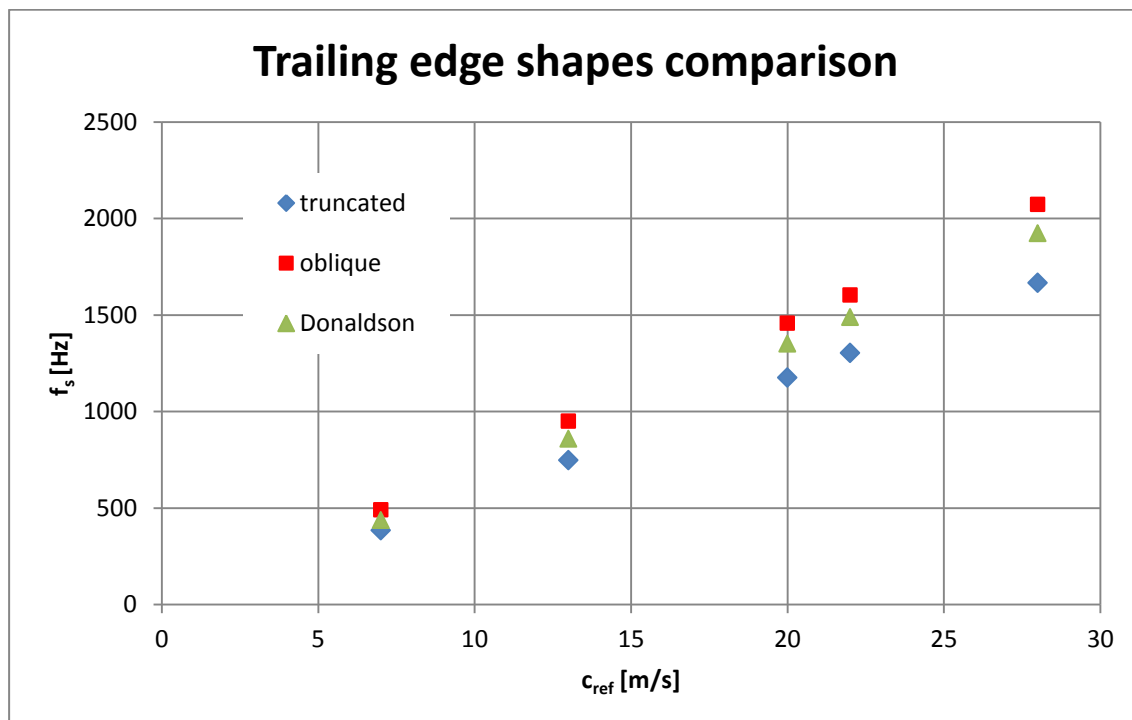


Fig. 5.20 Shedding frequency comparison for truncated, oblique and Donaldson trailing edges

Since the shedding frequency of the oblique trailing edge differs the most from the shedding frequency of the reference hydrofoil, this trailing edge appears to be the most suitable choice from the frequency point of view.

The relationship between Reynolds number and the normalized frequency, or Strouhal number, for the three trailing edges is presented in the Figure 5.21. In all three cases the Strouhal number is based on the reference hydrofoil trailing edge thickness $t_{ref} = 3.22$ mm. It can be seen that Strouhal number remains almost constant for the whole range of the Reynolds number.

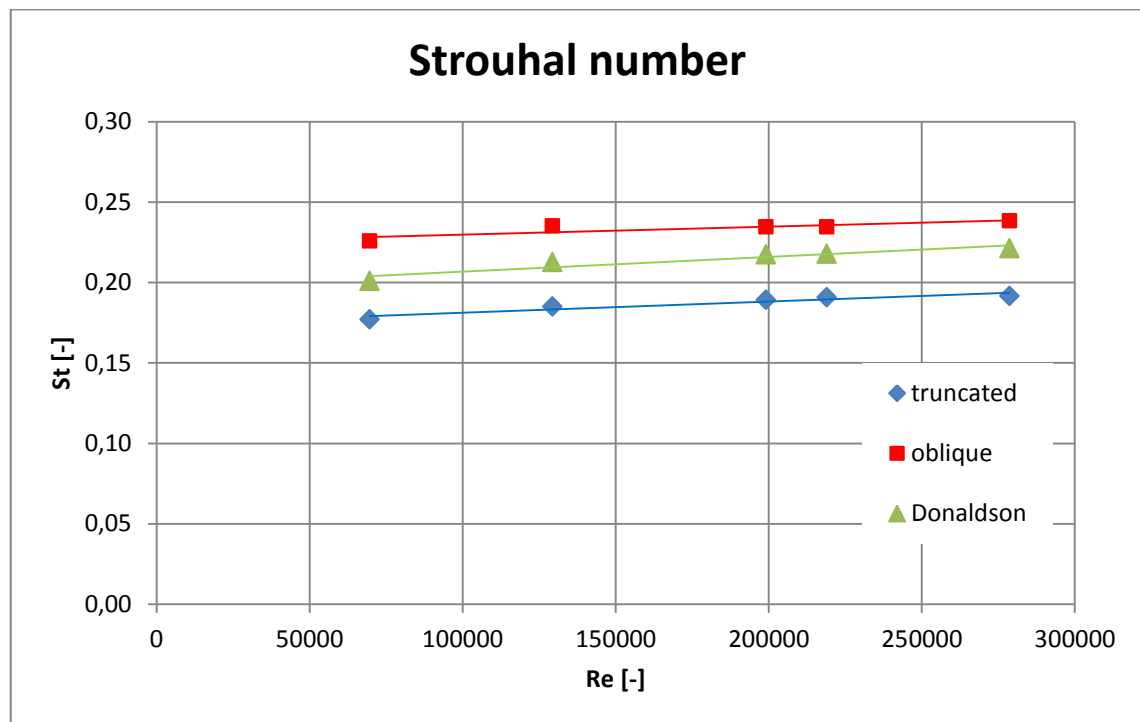


Fig. 5.21 Strouhal – Reynolds number relationship

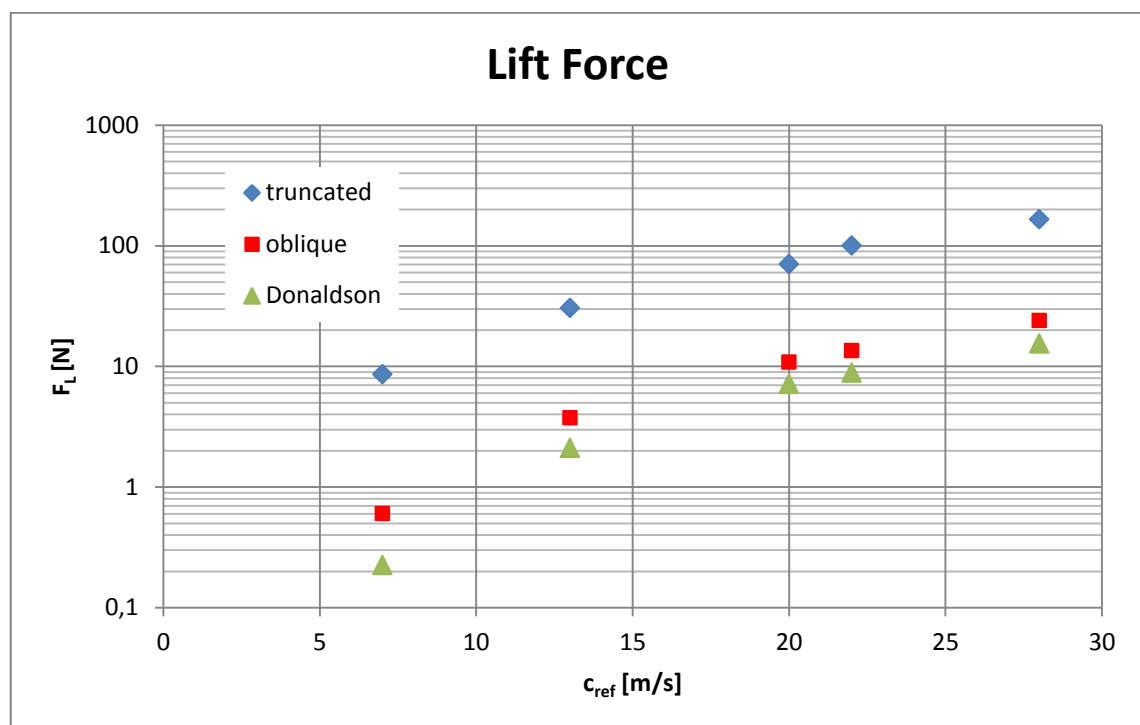


Fig. 5.22 Lift force comparison for truncated, oblique and Donaldson trailing edges

The comparison of the lift force amplitude of the three trailing edges is presented in Figure 5.22. Both oblique and Donaldson trailing edges cause significant decrease in the amplitude of the lift force which is positive from the fatigue-life point of view. Particularly the Donaldson trailing edge significantly reduces the amplitude, which is in agreement with literature. Fontanals [10] remarks that hydrofoils with this type of trailing edges generate a low amplitude vortex shedding which makes them quite interesting to avoid vortex induced vibrations and strong fluid-structure couplings.

6 ČBE ASSIGNMENT

The assignment by the company ČKD Blansko Engineering concerns the specific Francis turbine unit. Therefore the company provided the geometry of a model turbine stay vane, the inlet radius of the stay ring and the value of velocity on this inlet: The suction diameter of model turbine runner is $D_s = 322.5$ mm, the whole stay ring consist of 20 stay vanes, the stay ring inlet radius is $R_{in} = 272$ mm, the maximal thickness of the stay vane is $t_{max} = 6.15$ mm, the tangential inlet velocity $c_t = 6.9$ m/s and the radial inlet velocity $c_r = 2.7$ m/s.

6.1 CFD Simulation of ČBE Assignment

Spatial discretization:

The origin of the computational domain coordinate system is placed in the center of the stay ring. The inlet radius is $R_{in} = 272$ mm, the outlet radius is $R_{out} = 185$ mm. Since the whole stay ring consists of 20 stay vanes, the segment of the computational domain has the span of $\alpha = 18^\circ$. The shape of the computational domain is presented in Figure 6.1.

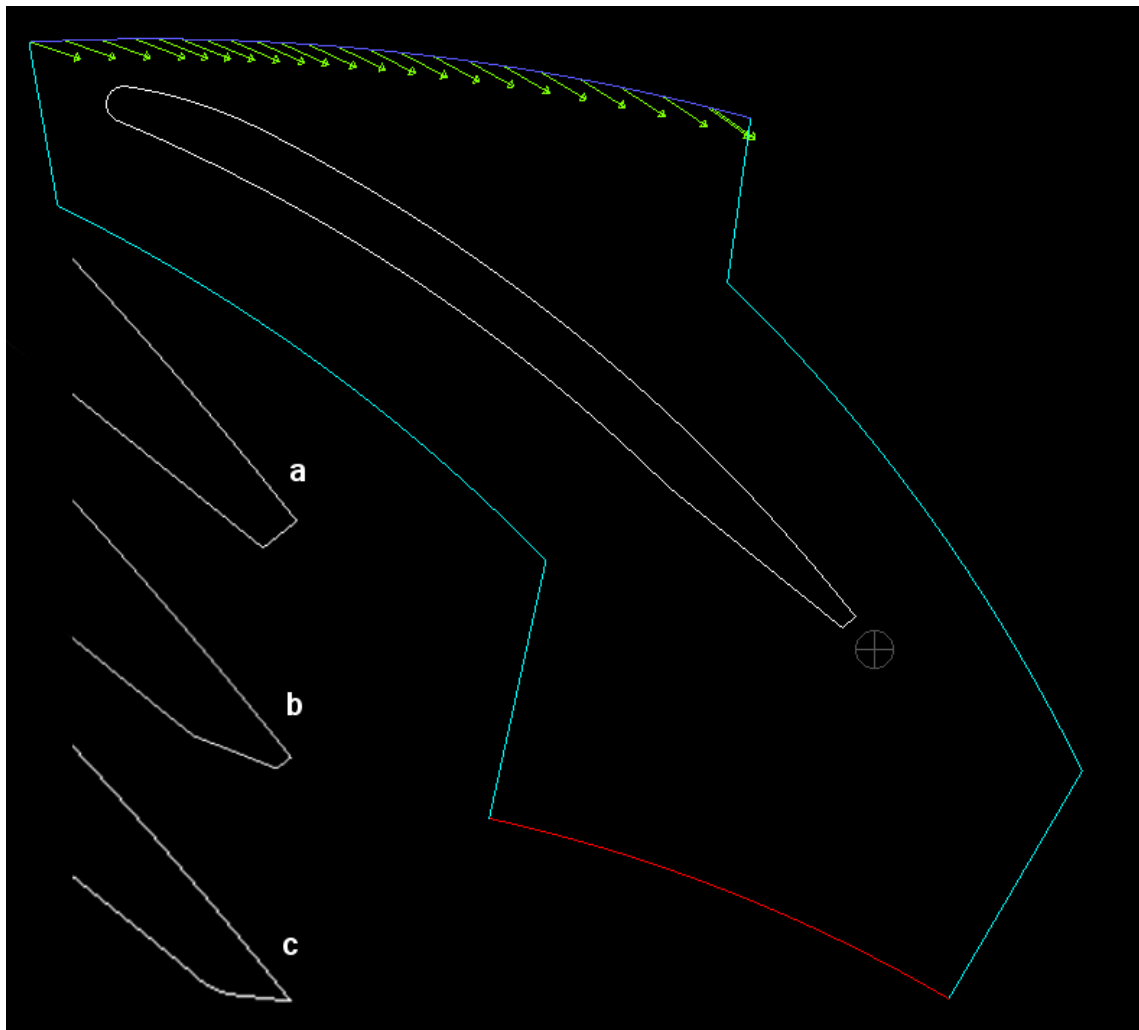


Fig. 6.1 Computational domain and the detail of trailing edges: a – original, b – oblique, c – Donaldson

In Figure 6.1 there are also the boundary conditions indicated by color: dark blue means velocity-inlet (the green arrows indicate the inlet-velocity profile), pale blue is the periodic boundary condition, red is pressure-outlet and white is wall. The periodic boundary condition significantly reduces the computational time, since it allows computing of only a segment of the whole geometry. *ANSYS Fluent* treats the flow at a periodic boundary as though the opposing periodic plane is a direct neighbor to the cells adjacent to the first periodic boundary. Therefore, when calculating the flow through the periodic boundary adjacent to a fluid cell, the flow conditions at the fluid cell adjacent to the opposite periodic plane are used. Periodic planes are always used in pairs. [9] There are basically two types of periodic boundary conditions: transitional and rotational. In this case the rotational one is used.

The Figure 6.1 also shows the details of individual trailing edges: a – the original ČBE stay vane trailing edge geometry; b – the first modification, oblique: the edge was chamfered at the angle 30° and the remaining trailing edge thickness is 0.8 mm; c – the second modification, Donaldson: the edge was chamfered at the angle 45° right from the upper edge and the connection to the vane profile is not sharp as in the case of first modification but round.

The point right behind the stay vane indicates the position where the y-velocity is monitored.

The solution of the assignment has some simplifications: since the flow in the spiral casing is three dimensional, the incoming flow angles differs for each stay vane and also the velocity varies from top to bottom of the spiral casing. Moreover the stay vane – guide vane cascade is not taken into account, which makes the computation somewhat dissimilar from the reality. However we believe that such a simplification is sufficiently accurate and allows the computation to be much more time-efficient.

For all the trailing edge geometries the realizable k- ϵ model was used as a turbulence model together with the non-equilibrium wall functions. All the meshes consist of 139 300 quadrilateral cells; the Map meshing type is used. The attempt was to make all the meshes as identical as possible so that the results could be subsequently compared.

Solver setting:

Boundary conditions are based on ČBE assignment.

On velocity-inlet bc the tangential velocity is $c_t = -6.9$ m/s and the radial velocity is $c_r = -2.7$ m/s; since the solver does not allow to define the tangential and radial component of the velocity, these components were transformed into c_x and c_y velocity components and read into the solver by means of *.prof* file. The turbulent intensity on velocity-inlet is 5 % and hydraulic diameter $D = 0.006$ m, based on maximal hydrofoil thickness.

On pressure-outlet bc the gauge pressure is $p = 0$ Pa, turbulent intensity 10 % and hydraulic diameter $D = 0.006$ m.

Sides of the computational domain are defined as rotational periodic bc.

The hydrofoil is defined as wall bc.

Solution methods:

Gradient – Least Squares Cells Based

Pressure – Standard

Momentum – QUICK

Turbulent Kinetic Energy k – Second Order UpwindTurbulent Dissipation rate ε – Second Order Upwind

Discretization of the unsteady term – Second Order Implicit

The time step was $\Delta t = 5\text{e-}6$ s.

6.2 CFD Results

The y-velocity was monitored in the point downstream of the hydrofoil with the coordinates $x, y, z = [0.085; 0.2; 0]$ m. In addition to the y-velocity, the lift and the drag coefficients were monitored to determine the lift force affecting the hydrofoil.

The Reynolds number based on the free stream velocity and the maximum hydrofoil thickness $t_{max} = 6.15$ mm is $Re = 45\,353$.

The comparison of shedding frequencies and the amplitude of the lift force is presented in Table 6.1. The Strouhal number values presented in this table is based on free stream velocity and the reference hydrofoil trailing edge thickness $t_{ref} = 2$ mm. Since the chord of the hydrofoil is not parallel with the x-axis but at an angle of 36.9° , the values of the lift force amplitude were obtained from the equation:

$$F = F_L * \cos 36.9^\circ + F_D * \sin 36.9^\circ \quad (6.1)$$

where F_L is obtained from the equation (5.1) and F_D is obtained from similar equation for drag coefficient:

$$C_D = \frac{F_D}{\frac{1}{2} * \rho * C_{ref}^2 * A} \quad (6.2)$$

where F_D is drag force, ρ is the fluid density, c_{ref} is the free stream velocity and A is the area of the hydrofoil. [9]

	f_s	St	dif.	F	dif.
trailing edge	Hz	-	%	N	%
original	576	0.155	0.00	53.5	0.00
oblique	714	0.193	23.96	1.25	-97.66
Donaldson	606	0.164	5.21	25.5	-52.34

Tab. 6.1 Comparison of shedding frequency and lift force amplitude for individual trailing edges

The comparison of vorticity and static pressure for the individual trailing edges is presented in Figure 6.2 and Figure 6.3 respectively.

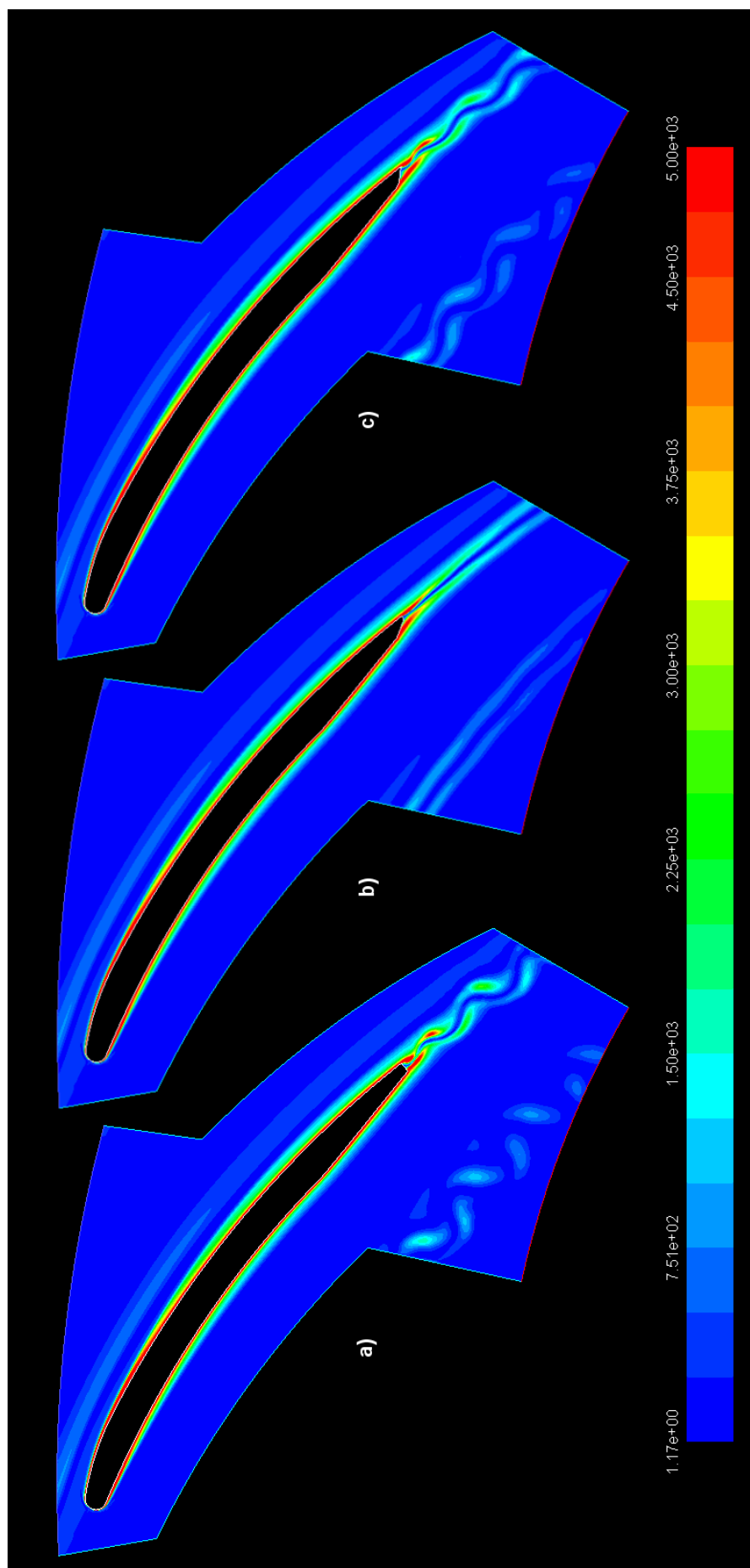


Fig. 6.2 Comparison of vorticity for the individual trailing edges:
a – original trailing edge; b – oblique; c – Donaldson

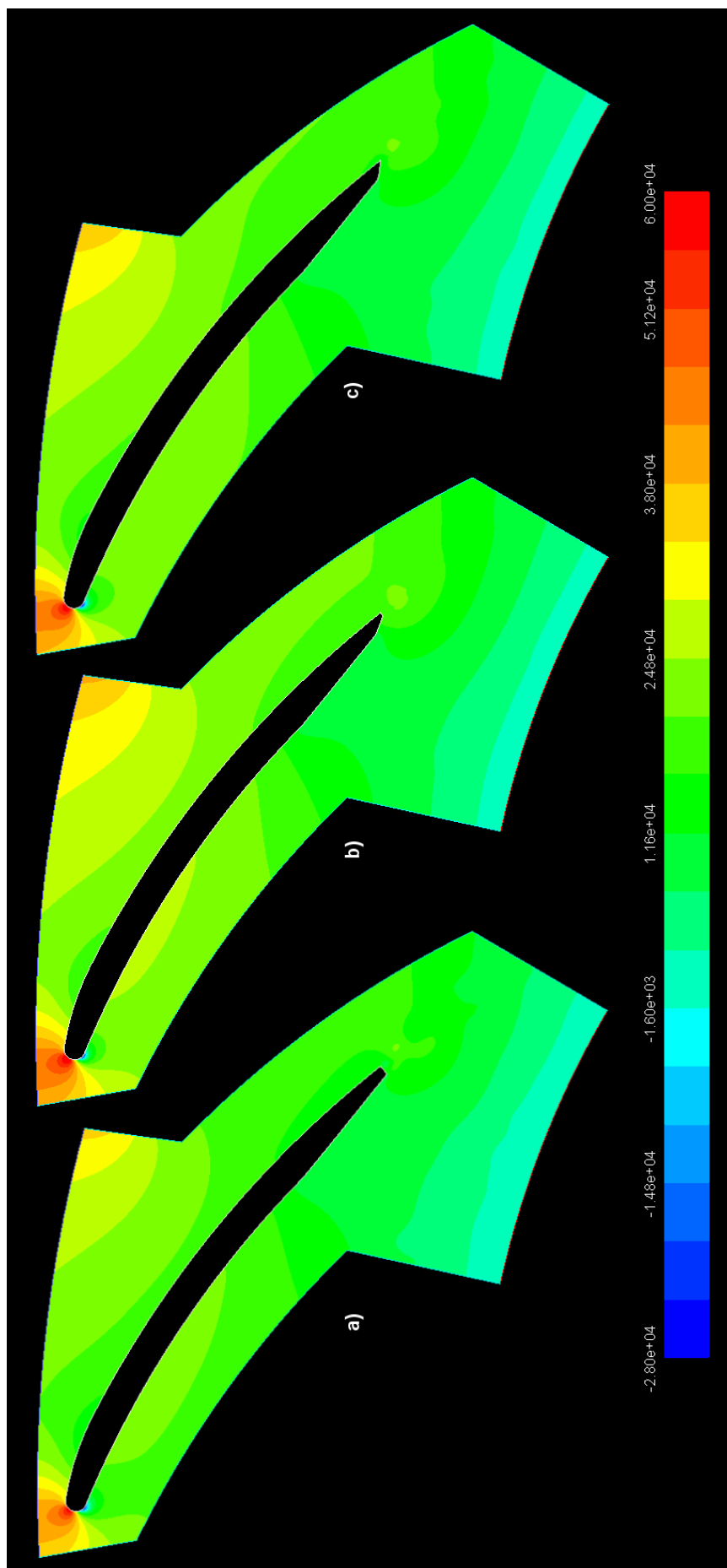


Fig. 6.3 Comparison of static pressure for the individual trailing edges:
a – original trailing edge; b – oblique; c – Donaldson

From the presented results it can be seen that both oblique and Donaldson trailing edges causes significant reduction of the lift force amplitude which is positive from the fatigue-life point of view. The Donaldson trailing edge, however, does not change the shedding frequency much. The difference of only 5 % does not guarantee the absence of lock-in phenomenon, which could be dangerous. It would be necessary to examine the natural frequency of the stay vane in the water to claim whether the difference of 5 % is sufficient.

The oblique trailing edge shows good results for both the shedding frequency and the lift force amplitude. The lift force amplitude is significantly reduced and the shedding frequency differs more than 20 % from the reference shedding frequency which definitely guarantees the absence of the lock-in phenomenon and so the lift force should not be further amplified.

III CONCLUSION AND PERSPECTIVES

7 CONCLUSION

The aim of the thesis was to find the optimal geometry of the specific stay vane trailing edge. The reason for this optimization is the fact that the original trailing edge geometry causes the periodic shedding of the vortices with the shedding frequency similar to the natural frequency of the stay vane. This coincidence which often presents itself by vane “singing” requires drainage of the unit and detailed inspection; in the worst case, it may cause severe damage to the stay vane and potentially to the runner.

The thesis is divided into three parts. The first part provides a qualitative description of periodic vortex shedding which is widely known as von Kármán vortex street and of the related topics such as Strouhal number, lock-in phenomenon and hydro-turbine stay vane cracking caused by vortex induced vibration. This part serves as an introduction to the problem.

The second part consists of two test cases and the ČBE assignment. The test cases serve as a tool for the CFD solver tuning: the first test case employs the experiment of vortex shedding past square cylinder executed by Lyn in 1992. The result of the experiment is accessible in the ERCOFTAC database. There were two turbulence models used for CFD analysis of this test case: realizable k - ϵ and Reynolds Stress model. Both of these were used in two- and three-dimensional approach. The closest agreement with the experiment showed 2D realizable k - ϵ model.

The second test case is based on the flow past NACA 0009 hydrofoil executed by Zobeiri in 2012. This test case should prove that the CFD solver is sensitive to the trailing edge geometry modification. Zobeiri measured wide range of velocities on hydrofoils with three different trailing edges: blunt truncated (which was chosen as a reference one), oblique (beveled at 30°) and Donaldson (beveled at 45°). It is believed that asymmetric trailing edges cause a spatial phase shift of the upper and lower vortex at their generation stage which leads to their partial elimination. Since the CFD is unable to respond to lock-in condition, five values of velocity that are not affected by the lock-in were chosen for the CFD computation. For the nature of the vortex shedding is three-dimensional, the 3D approach of realizable k - ϵ model was employed. It has not given, however, any better results and equally so the SST k - ω model has not proven to be any better. Moreover, these two approaches are very time consuming. Therefore, in order to obtain time-efficient computation, the 2D realizable k - ϵ model was employed which showed good agreement with the experimental results.

On the basis of these two test cases, the ČBE assignment was resolved. ČBE company provided the geometry of a specific stay vane for a model Francis turbine with the runner suction diameter $D_s = 322.5$ mm. maximum thickness of the stay vane $t_{max} = 6.15$ mm. The computation was carried out by means of 2D realizable k - ϵ model. Two trailing edge modifications were compared with the original ČBE geometry. The first modification is oblique: the edge is chamfered at the angle 30° and the remaining trailing edge thickness is 0.8 mm; the second modification is Donaldson-like: the edge is chamfered at the angle 45° right from the upper edge and

the connection to the vane profile is not sharp as in the case of first modification but round. The details of the individual trailing edges are presented in Figure 6.1.

The modifications were subsequently evaluated from two points of view: first, the shedding frequency was obtained by means of Fast Fourier Transform (FFT) of monitored time-varying y -velocity values. And second, the lift force amplitude was determined from time-varying lift coefficient values.

As for the lift force amplitude, both modifications showed considerable reduction of the amplitude, but as for the shedding frequency, the Donaldson trailing edge showed only 5 % difference from the original trailing edge which could prove insufficient. Such a small difference does not guarantee the absence of lock-in condition, which causes the amplification of the resulting lift force. The oblique trailing edge showed more than 20 % higher shedding frequency than the original trailing edge and so the lock-in most likely will not occur. Therefore the oblique trailing edge modification proves to be optimal from both shedding frequency and lift force amplitude points of view.

8 PERSPECTIVES

There is also a more profound approach to the solution of vortex shedding: the stay vanes or guide vanes can be drilled through from the upper to the lower side, so that the lower side boundary layer would move to the upper side of the vane similarly as it is done in case of airfoil slotted flaps.

Another approach is discussed by Lewis et al. [15]: he suggests the usage of additional water jets in the vanes. The water should be supplied via vane pivot and led through the channels to the trailing edge as shown in Figure 8.1.



Fig. 8.1 Water jets in a vane [15]

Such water jet can partially eliminate the vortices downstream the vane and so have a positive impact on vortex induced vibration. However, the question is whether such a solution would be economical, since the channels demand additional workshop effort and the chamfering of the trailing edge seems to be sufficient.

These can be the directions of further vane investigation.

ABBREVIATIONS AND SYMBOLS USED

Abbreviation:

bc	boundary condition
CFD	Computational Fluid Dynamics
ČBE	ČKD Blansko Engineering
EPFL	École Polytechnique Fédérale De Lausanne
ERCOFTAC	European Research Community On Flow, Turbulence and Combustion
FFT	Fast Fourier Transform
LDV	Laser Dopler Velocimetry
NACA	National Advisory Committee for Aeronautics
QUICK	Quadratic upstream interpolation for convective kinematics
RSM	Reynolds Stress Model
SST	Shear Stress Transition

Symbol:	Name:	Unit:
a	stream-wise distance of nearby vortices	m
b	cross-stream distance of the two vortex rows	m
c_D	drag coefficient	1
c_L	lift coefficient	1
c_{\max}	maximum inlet velocity	m/s
c_n	normal velocity	m/s
c_r	radial inlet velocity	m/s
c_{ref}	free stream velocity	m/s
c_t	tangential inlet velocity	m/s
c_x	x-velocity	m/s
c_y	y-velocity	m/s
d	side length	m
D	characteristic body dimension	m
D_s	suction diameter of a runner	m
F_D	drag force	N
F_L	lift force	N
f_s	vortex shedding frequency	Hz
h_t	hydrofoil trailing edge thickness	m
L	chord length	m
p	pressure	Pa
p_{ref}	static pressure	Pa
R_a	surface roughness	μm
Re	Reynolds number	1
R_{in}	inlet radius is	m
R_{out}	outlet radius is	m
St (Sh/ Sth)	Strouhal number	1

t_{\max}	maximal thickness of the stay vane	m
t_{ref}	reference hydrofoil trailing edge thickness	m
y	distance to the nearest wall	m
y^+	dimensionless distance from the wall	1
δ	boundary layer thickness	m
μ	dynamic viscosity	Pa.s
τ_w	wall shear stress	Pa
u_τ	friction velocity	m/s
ν	kinematic viscosity	m ² /s
ρ	density	kg/m ³

REFERENCES

- [1] AUSONI, P. *Turbulent vortex shedding from a blunt trailing edge hydrofoil*. Lausanne: EPFL, 2009, PhD thesis, N°4475.
- [2] AUSONI, P., et al. Kármán vortex shedding in the wake of a 2D hydrofoil: Measurement and numerical simulation. *IAHR International Meeting of the Workgroup on Cavitation and Dynamic Problems in Hydraulic Machinery and Systems*. Barcelona, Spain: 2006.
Accessible via < <http://infoscience.epfl.ch/record/88122>>
- [3] BAJER, J. *Mechanika 3*. Olomouc: chlup.net, 2012. ISBN 978-80-903958-5-5.
- [4] BEARMAN, P.W. Vortex Shedding from Oscillating Bluff Bodies. *Annual Review of Fluid Mechanics*, 1984, vol. 16, no. 1. pp. 195-222.
- [5] BREKKE, H. New Trends in Technologies: Devices, Computer, Communication and Industrial Systems. Sciyo, 2010. ISBN 978-953-307-212-8, 454 pages. Chapter 12: A Review on Oscillatory Problems in Francis Turbines. pp.217-232. Accessible via <<http://www.intechopen.com>>
- [6] CABANA, M., MASSOULIER, C. Von Karman Vortex Street. *Hydraulique et Mécanique des Fluides*. [online]. 2003. Accessible via <<http://hmf.enseeiht.fr/travaux/CD0203/travaux/optmfn/gpfmho/02-03/index.htm>>
- [7] DÖRFLER, P., SICK, M., COUTU, A. *Flow-induced pulsation and vibration in hydroelectric machinery*. London: Springer, 2012. pp. 111-127 & 213-219. ISBN 978-1-4471-4251-5.
- [8] ELOY, C. Optimal Strouhal number for swimming animals. *Journal of Fluids and Structures*, 2012, vol. 30. pp. 205-218. Accessible via < <https://www.irphe.fr/~eloy/PDF/JFS2012.pdf>>
- [9] *FLUENT User's Guide*. [online]. Accessible via < https://www.sharcnet.ca/Software/Fluent6/html/ug/main_pre.htm> [cit.2015-05-13].
- [10] FONTANALS, A., et al. Boundary layer effects on the vortex shedding in a Donaldson-type hydrofoil. *IAHR Symposium on Hydraulic Machinery and Systems*. Montréal, Canada: 2014.
Accessible via <<http://iopscience.iop.org/1755-1315/22/3/032045>>
- [11] GERRARD, J.H. The Mechanics of the formation region of vortices behind bluff bodies. *Journal of Fluid Mechanics*, 1966, vol. 25, issue 2, pp. 401-413.
- [12] GOLDWAG, E., BERRY, D.G. Von Karman Hydraulic Vortexes Cause Stay Vane Cracking on Propeller Turbines at the Little Long Generating Station of

- Ontario Hydro. *Journal of Engineering for Power*, 1968, vol. 90, no. 3. pp. 213–217.
- [13] GUMMER, J.H., HENSMAN, P.C. A review of stayvane cracking in hydraulic turbines. *International Water Power and Dam Construction*, 1992, vol. 44, no. 8. pp.32-42.
- [14] LARRAGUETA, J. Von Karman street part 2. *Basic Air Data Instrument* [online]. March, 2014. [cit. 2015-05-04]. Accessible via <<http://basicairdata.blogspot.cz/2014/03/von-karman-street-part-2.html>>
- [15] LEWIS, B.J., et al. Wicket gate trailing-edge blowing: A method for improving off-design hydroturbine performance by adjusting the runner inlet swirl angle. *IAHR Symposium on Hydraulic Machinery and Systems*. 2014. Accessible via <http://iopscience.iop.org/1755-1315/22/1/012021/pdf/1755-1315_22_1_012021>
- [16] LOCKEY, K.J., et al. Flow-induced vibrations at stayvanes: experience on site and CFD simulations. *Hydropower & Dams*, 2006, issue 5. pp. 102-106.
- [17] LYN. Vortex Shedding Past Square Cylinder. 1992 [cit. 2015-02-11]. Accessible via <<http://cfd.mace.manchester.ac.uk/ercoftac/index.html>>
- [18] NIELSEN, T.K., ANTONSEN, Ø. CFD simulation of von Karman vortex shedding. *IAHR Work Group on The Behaviour of Hydraulic Machinery under Oscillatory Conditions*. Stuttgart, Germany. Accessible via <<http://www.ihs.uni-stuttgart.de/fileadmin/IHS-Startseite/Institut/Veranstaltungen/IAHR/Nielsen.pdf>>
- [19] SCHLICHTING, H., GERSTEN, K. *Boundary Layer Theory*. 8th Revised and Enlarged Edition. Berlin: Springer, 2000. ISBN 3-540-66270-7.
- [20] STEVE, M.S. Hydraulic Turbines. *Slideshare.net* [online]. 2013. Accessible via <<http://www.slideshare.net/msstevesimon/hydraulic-turbines-24891748>>
- [21] VAN DYKE, M. *An Album of Fluid Motion*. 4th printing, 1988. Stanford: The Parabolic Press, c1982. ISBN 0-915760-02-9.
- [22] VÍT, J. *Modelování nestacionárního proudění v úplavu*. Brno: VUT, FSI, 2003. Master thesis. 54 pages.
- [23] VU, T., et al. Unsteady CFD Prediction of von Kármán Vortex Shedding in Hydraulic Turbine Stay Vanes, *Proceeding of Hydro*, 2007.
- [24] ZOBEIRI, A. *Effect of Hydrofoil Trailing Edge Geometry on the Wake Dynamics*. Lausanne: EPFL, 2012, PhD thesis, N°5218.
- [25] ZOBEIRI, A., et al. Vortex Shedding from Blunt and Oblique Trailing Edge Hydrofoils. *IAHR International Meeting of the Workgroup on Cavitation and Dynamic Problems in Hydraulic Machinery and Systems*. Brno: 2009. Accessible via <<http://infoscience.epfl.ch/record/142244>>